# A Quantum Mechanical Study of Lithium Titanium Oxide for Lithium Recovery

## Sustainable and High-Selectivity Extraction in Complex Brines

ME55035: ME-EFPT MSc Thesis

A.M. Guluma

Delft University of Technology

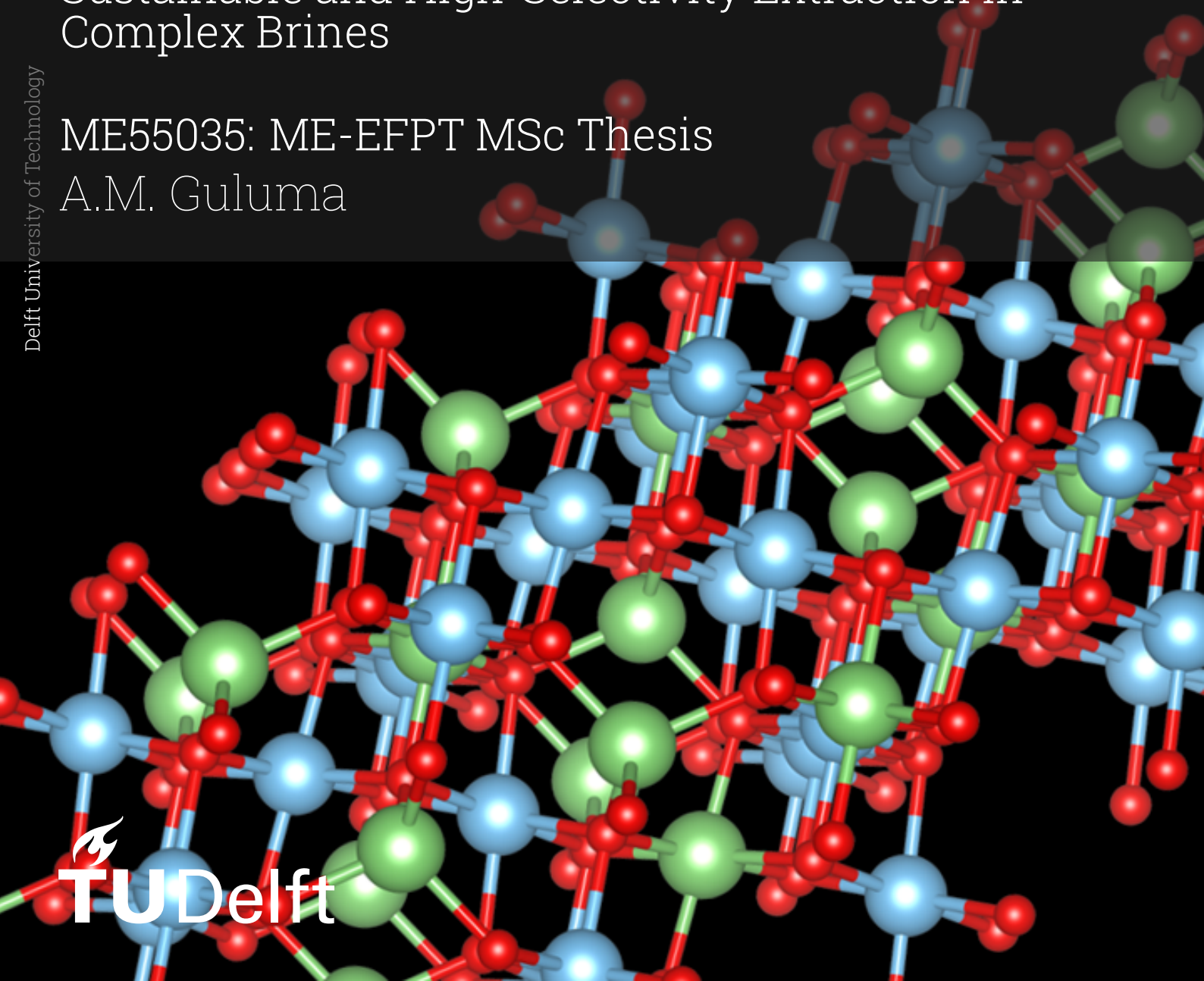

TU Delft

# A Quantum Mechanical Study of Lithium Titanium Oxide for Lithium Recovery

## Sustainable and High-Selectivity Extraction in Complex Brines

by

A.M. Guluma

Supervisors: Dr. O. Moultos
Dr. A. Vasileiadis

Project Duration: January 2025 - September 2025
Faculty: Faculty of Mechanical Engineering, TU Delft
Student Number: 4795172

TU Delft

# Abstract

The accelerating demand for lithium in energy storage technologies is straining conventional mining and evaporation methods, driving interest in selective recovery from low-grade and chemically complex brines. This thesis evaluates spinel lithium titanium oxide ($Li_4Ti_5O_{12}$, LTO) as a lithium-ion sieve using density functional theory (DFT) to provide atomistic insight into its thermodynamic stability, structural evolution, and ion-exchange kinetics. Two objectives guided this work: (i) establishing the phase stability and electrochemical response of LTO during lithium extraction with proton incorporation, and (ii) identifying and quantifying lithium and proton migration pathways that govern ion-exchange rates.

DFT thermodynamics show that proton substitution stabilizes delithiated frameworks relative to vacancy states, shifting the voltage profile to lower potentials and yielding solid-solution behavior with near-zero-strain structural evolution. Nudged elastic band (NEB) analysis revealed a kinetic hierarchy: lithium diffuses efficiently via the 8a $\rightarrow$ 16c $\rightarrow$ 8a pathway, where the 16c site acts as a kinetic bridge, while octahedral 16d lithium remains kinetically trapped. In contrast, proton migration exhibits substantially higher barriers ($\geq 1.9$ eV) that scale with geometric path length, indicating that $H^+$ mobility is the likely rate-limiting step in the exchange cycle.

These findings reconcile experimental observations of structural robustness yet sluggish adsorption–desorption kinetics in LTO sieves. They highlight three design levers for improving performance: enhancing 16c accessibility to accelerate $Li^+$ diffusion, engineering shorter or lower-barrier proton pathways, and maintaining homogeneous lithiation for optimal sieving rates. Together, this study establishes a basis for rational improvements to spinel LTO sieves and sets a computational–experimental agenda for advancing sustainable and economic lithium recovery from challenging brines.

# Contents

# 1

# Introduction

## 1.1. Motivation for Lithium Recovery

Lithium (Li) is an essential element in modern clean-energy technologies, most notably in lithium-ion batteries (LIBs) used in electric vehicles and large-scale energy storage [1]. This is due to LIBs' unique combination of high energy density, long cycle life, high power output, and low self-discharge rate, which has led to lithium being referred to as the "white gold" of the energy transition [2, 3]. As global initiatives pivot toward a low-carbon economy, the demand for lithium is expected to rise significantly [4]. Recent assessments of critical metals supply and demand indicate that by 2030, lithium consumption could strain existing extraction capacity [5]. This tension between supply and demand, visualized in Figure 1.1, underscores the urgent need to streamline lithium recovery methods and improve the availability of Li.

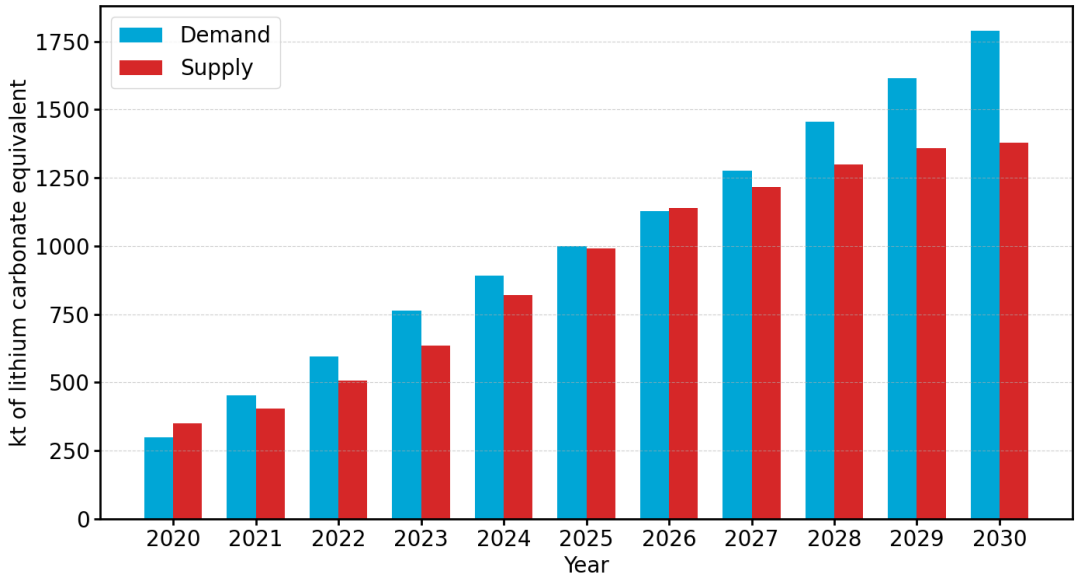


**Figure 1.1:** Projected lithium carbonate equivalent supply and demand [4].

Despite ongoing expansion in production, conventional extraction approaches face considerable hurdles. Solar pond evaporation of brines, for instance, requires extensive land areas, water usage, and processing times, while hard-rock mining is energy-intensive and costly [6]. Moreover, in challenging feedstocks such as high-magnesium brines or those with low lithium concentrations, selective recovery of lithium remains technically and economically difficult [7]. To address these limitations, there is growing interest in the development of recovery materials that enable more sustainable, efficient, and selective extraction [8].

## 1.2. The Role of Molecular Modeling

Several factors constrain experimental approaches to understanding and improving lithium-recovery materials [9]. First, they tend to be both expensive and slow. Second, there is considerable difficulty in isolating atomic-scale variables. Laboratory setups rarely allow for perfect control over conditions such as pH, ionic strength, or dopant concentration, making it challenging to draw precise conclusions. Third, the mechanisms involved are often transient. Capturing lithium intercalation or adsorption pathways in real time is experimentally demanding and typically requires specialized instrumentation.

Atomic modeling offers powerful tools to overcome these limitations. It provides molecular-level insights through simulations such as density functional theory, allowing researchers to predict lattice distortions, surface binding energies, and diffusion barriers [9, 10, 11]. These methods also help predict key thermodynamic and kinetic properties, offering understanding of how lithium interacts with intercalation sites, the energetics of insertion, and the potential effects of dopants on material performance. Furthermore, computational modeling significantly accelerates material screening. Before committing to labor-intensive and costly synthesis efforts, one can computationally evaluate new materials, doping strategies, or structural modifications to progress adsorption capacity and selectivity.

## 1.3. Research Objectives

This thesis aims to better understand the ion-exchange behavior of the lithium recovery material spinel lithium titanium oxide through the Density Functional Theory molecular modeling method, specifically:

1. Establish the phase stability and electrochemical response of spinel $Li_4Ti_5O_{12}$ during coupled lithium extraction and proton incorporation by employing first-principles thermodynamics to map composition-dependent voltages, lattice evolution, and phase behavior.
2. Identify and quantify the atomistic ion-migration processes that govern $Li^+$ and $H^+$ transport in the bulk lattice, determining rate-limiting pathways and their activation barriers so that kinetic limitations can be linked directly to underlying site preferences.

Ultimately, by clarifying key adsorption pathways and identifying how they can be manipulated at the atomic scale, it is hoped to guide targeted experiments and inform the development of efficient lithium-recovery solutions from brines, accelerating material improvements for large-scale lithium recovery.

# 2

# Literature Review

## 2.1. Lithium-Rich Brines

As illustrated in Figure 2.1, the majority (around 65%) of current commercial lithium production originates from brine sources [12]. These liquids (continental brines, geothermal, and oilfield brines) differ significantly in composition, economic viability, and environmental footprint. In general, higher lithium concentrations and chemically dissimilar ionic compositions can translate into more cost-effective lithium extraction processes; however, brines with favorable chemistry are often geographically or logistically limited. Conversely, more abundant or widely distributed sources, such as seawater and oilfield brines, have lower lithium content, creating a challenge for profitable lithium recovery.

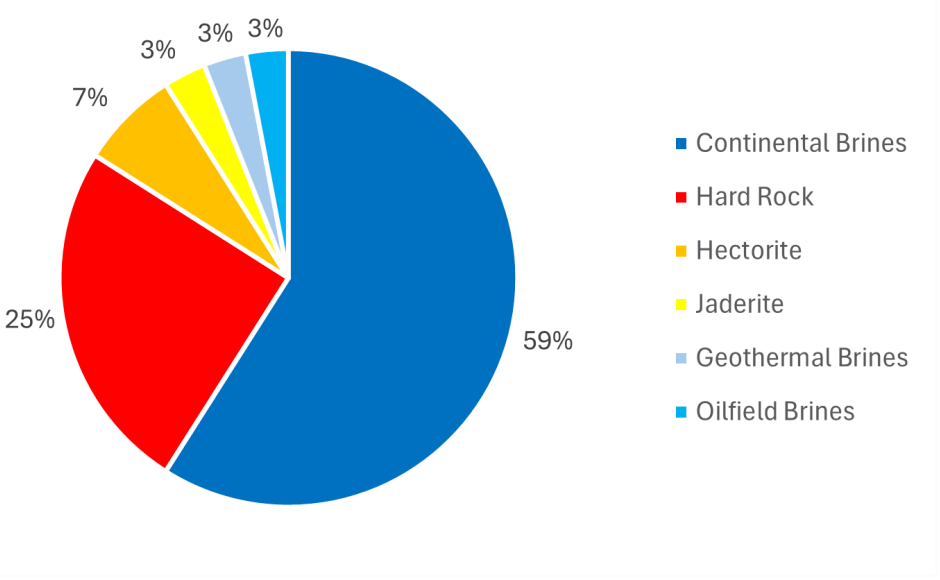


**Figure 2.1:** Distribution of sources for current lithium production, highlighting that the majority (65%) of lithium is extracted from brine sources [12].

Table 2.1 summarizes the brine types discussed in this chapter. Each source offers a route to produce battery-grade lithium, but no single option is unequivocally superior. For instance, continental brines typically have higher lithium content, yet they are heavily scrutinized for water usage and environmental impact [20]. Geothermal and oilfield brines may offer synergies with existing energy infrastructure, though their ionic compositions can limit opportunities for selective lithium extraction [14, 15]. Seawater is the most abundant reservoir of lithium on the planet, but its extremely low lithium concentration demands highly selective technologies [16]. Meanwhile, brines from spent lithium-ion batteries hold

**Table 2.1:** Comparison of lithium-rich brines, summarizing the trade-offs between ease of lithium recovery, environmental impact, and integration potential across conventional and alternative brine sources.

| Brine | Li Range (mg/L) | Mg/Li Ratio | Advantages | Challenges |
|---|---|---|---|---|
| **Continental Brines** | Up to ∼1,800 | 1 – 20 | Higher Li concentration; established evaporation technology | Water-intensive; yield varies by chemistry; large solid waste streams [13] |
| **Geothermal Brines** | 125 – 480 | 0.03 – 2.5 | Possible co-production of thermal energy; on-site integration | Complex ionic mixtures; concentrations lower than continental brines [14] |
| **Oilfield Brines** | ∼28 – 140 | 2 – 30 | Globally abundant; partial use of existing infrastructure | Often high in interfering ions; not yet widely commercialized [15] |
| **Seawater** | ∼0.17–12 | 7,500 – 8,000 | Virtually unlimited volume | Extremely low Li; intense Na/Mg competition [16] |
| **Battery Leachate** | ∼3,000–5,500 | Impurities only | Fewer competing ions; circular-economy potential | Industrial recycling usually targets Co/Ni; Li often under-recovered [17, 18, 19] |

significant promise for a circular-economy approach, but they must be synthesized, and most commercial recyclers still focus on recovering transition metals like cobalt and nickel, leaving lithium as an afterthought [21].

A notable challenge across many of these sources is the presence of large amounts of interfering ions, especially magnesium. Magnesium poses a significant challenge in lithium extraction because the elements occupy diagonal positions in the periodic table, leading to similar chemical properties, including atomic radius and mass, and to the fact that their carbonate and hydroxide compounds tend to co-precipitate [22]. With high Mg/Li ratios (above 6), standard extraction methods, such as precipitation, struggle to differentiate Li from Mg effectively [7]. This not only drives up costs and processing times, but it can also reduce lithium recovery yields, ultimately impacting the viability of the extraction process [13, 20].

Taken together, these observations underscore a trade-off: natural brines that exhibit higher lithium concentrations and fewer interfering ions often appear in limited quantities and are concentrated in specific regions, whereas more plentiful or widely distributed brines are highly dilute and contain very high Mg/Li ratios. In a similar vein, brines from spent lithium-ion batteries can provide elevated lithium content and fewer competing ions; yet recovering lithium via specialized hydrometallurgical processes remains costly and is not always prioritized industrially, limiting the total volume of Li that is reclaimed from this pathway. Overcoming these conflicting factors will require technological advancement and a shift in lithium recovery priorities to ensure a stable, cost-effective, and sustainable supply, particularly as global demand surges. The subsections below further explore the composition, challenges, and technological opportunities unique to each brine source.

### 2.1.1. Continental Brines

As seen in Figure 2.1, continental brines, also known as salt lakes, are the world's most utilized lithium source, offering several economic and operational advantages [12]. Chief among these is the low-cost and high-margin characteristics of evaporitic technology, which relies on solar and wind-driven evaporation to concentrate brines pumped into large, shallow ponds before further recovery [20].

However, despite being considered less environmentally harmful than hard rock mining, lithium extraction from continental brines comes with sustainability disadvantages [6]. The process is extremely water-intensive, requiring on average 500,000 liters of brine and an additional 5,000 to 50,000 liters of freshwater per ton of battery-grade lithium carbonate produced [20]. Moreover, evaporitic extraction generates a vast amount of solid salt waste- over 115,000 kilograms per ton of lithium carbonate. The process is also slow, taking one to two years to complete depending on climate conditions, and therefore may not be suited to meet rapid shifts in demand.

Additionally, lithium recovery yields are variable and can be as low as 50%, particularly in brines with high magnesium concentrations, which require chemical treatment beyond evaporation, reducing economic viability [20]. This depends on the brine composition of the deposit, as the specific ionic composition influences the technological approach and the feasibility of extraction. Table 2.2 below demonstrates the variability in ionic concentrations found in a range of continental brine deposits. It should be noted that a Li extraction from a brine with a Mg/Li ratio greater than 10 has yet to be made profitable [13].

**Table 2.2:** Chemical composition **(mg/L)** of different continental brine deposits [13, 7].

| **Deposit** | **Li** | **K** | **Mg** | **Ca** | **$SO_4$** | **B** | **Mg/Li** |
|---|---|---|---|---|---|---|---|
| Salar de Atacama | 1835 | 22626 | 11741 | 379 | 20000 | 783 | 6.4 |
| Salinas Grandes Salt Flats | 775 | 9289 | 2117 | 1450 | 1036 | 232 | 2.7 |
| Dead Man's Salt | 744 | 7404 | 1020 | 636 | 10236 | 420 | 1.4 |
| Salar de Hombre Muerto | 745 | 8318 | 1781 | — | 8642 | — | 2.4 |
| Silver Peak | 245 | 5655 | 352 | 213 | 7576 | 85 | 1.4 |
| Salar de Olaroz | 774 | 6227 | 2005 | 416 | 18630 | 1136 | 2.6 |
| Cauchari Salt Flat | 618 | 5127 | 1770 | 476 | 19110 | 1360 | 2.9 |
| Salar de Uyuni | 424 | 8719 | 7872 | 557 | 10342 | 2442 | 18.6 |
| Rincon Salt Flats | 397 | 7513 | 3419 | 494 | 12209 | 331 | 8.6 |
| Maricunga Salt Flat | 1036 | 8869 | 8247 | 11919 | 1095 | 634 | 8.0 |
| Da Qaidam Salt Brine | 1000 | 73090 | 44080 | 8320 | 3078 | — | 41.6 |

Continental brines also present broader geopolitical challenges; the majority of the world's lithium production originates from just eight sites, including Salar de Atacama, Salar del Hombre Muerto, and Salar de Olaroz [15]. These geographic concentrations, visualized by the blue circles in Figure 2.2, and the finite nature of continental brines, raise concerns over supply security and the resilience of global lithium supply chains in the face of rising demand.

### 2.1.2. Geothermal Brines

Geothermal brines have emerged as a promising alternative lithium source, offering a pathway toward diversifying global lithium supply chains. These brines, byproducts of geothermal power generation, can be processed before reinjection into the reservoir to produce lithium alongside heat and electricity [24].


**Figure 2.2:** World map showcasing the geographical concentration of continental brines and relative sizes of lithium in reserve [23].

**Table 2.3:** Composition **(mg/L)** of the only economically viable lithium-extraction geothermal brine deposits in Europe. [14].

| Location | Li | Na | K | Ca | Mg | Cl | $SO_4$ | Sr | B | Mg/Li |
|---|---|---|---|---|---|---|---|---|---|---|
| Campi Flegrei | 480 | 85200 | 43400 | 54000 | — | 314000 | — | — | 231 | — |
| Cesano | 350 | 63600 | 21400 | 43 | 12 | 37000 | 91010 | — | 2448 | 0.03 |
| Groß Schönebeck | 201 | 39100 | 3910 | 56100 | 437 | 167000 | 139000 | 1928 | — | 2.17 |
| Molasse Basin | 143 | 18700 | 1140 | 880 | 351 | 30800 | 1852 | — | — | 2.45 |
| Upper Rhine Graben | 182 | 28200 | 4000 | 7700 | 80 | 64500 | 130 | 143 | 40.8 | 0.44 |
| South Crofty Mine | 125 | 4300 | 180 | 2470 | 73 | 11500 | 11500 | 125 | 11.0 | 0.58 |

Several technical and economic challenges persist; the chemical compositions, shown in Table 2.3, of geothermal brines, particularly high concentrations of interfering ions such as Na and K, may necessitate brine purification before lithium can be selectively recovered [25]. Moreover, lithium concentrations in geothermal brines are generally lower than those in high-grade continental brines, increasing the volume of fluid that must be processed in order to obtain a given amount of lithium [13, 14]. Additionally, uncertainties regarding the long-term stability of lithium concentrations in geothermal reservoirs, combined with the need for periodic drilling to maintain production, pose operational and environmental concerns [25]. The European geothermal brines detailed in Table 2.3 represent the only known reservoirs on the continent currently deemed capable of economically viable lithium recovery [14].

Despite these limitations, geothermal brines offer a potentially lower-impact alternative when optimized with renewable energy inputs and site-specific process designs.

### 2.1.3. Oilfield Brines

Oilfield brines have the potential to serve as an alternative lithium source due to their availability and integration with existing infrastructures. These brines are produced as a byproduct during crude oil and natural gas extraction, making them an attractive candidate for resource recovery [15]. It has been estimated that nearly 40 million $m^3$ of oilfield brine is produced daily [26]. However, currently, only 1% of this amount is repurposed [27]. One of the key challenges in doing so lies in the composition of brines; elevated concentrations of other dissolved elements, and relatively low lithium content, as quantified in Table 2.4, can impact the feasibility of lithium recovery. It again should be noted that a Li extraction from a brine with a Mg/Li ratio greater than 10 has not yet been made profitable [13].

**Table 2.4:** Composition **(mg/L)** of selected oilfield brine [15].

| Location | Li | Na | K | Ca | Mg | Cl | $SO_4$ | Sr | Br | Mg/Li |
|---|---|---|---|---|---|---|---|---|---|---|
| Qianjiang Basin | 119 | 85800 | 1440 | 1240 | 240 | 132900 | 4620 | — | 371 | 2.02 |
| Smackover | 445 | 71400 | 8340 | 45700 | 2970 | 196100 | 550 | 2980 | 5850 | 6.67 |
| Carboniferous | 81 | 53000 | 3060 | 36000 | 2538 | 165000 | 2090 | 2347 | — | 31.33 |
| Leduc Fm. | 140 | 61000 | 3900 | 22800 | 2000 | 145000 | 220 | 660 | 436 | 14.29 |
| Swan Hills | 118 | 69600 | 4600 | 24370 | 2250 | 147400 | 210 | 845 | 462 | 19.07 |
| Wolfcamp Shale | 28 | 45100 | 900 | 2770 | 380 | 75400 | 650 | 421 | 639 | 13.57 |
| Bakken | 57 | 91700 | 5310 | 17000 | 1340 | 177800 | 760 | 1450 | 874 | 23.51 |
| Marcellus Formation | 127 | 43700 | 870 | 18950 | 1670 | 116100 | 50 | 3693 | 1126 | 13.15 |

### 2.1.4. Seawater

Seawater represents the world's largest lithium reservoir, with an estimated 230 billion tons of lithium, vastly exceeding the approximately 62 million tons available in land-based reserves [28]. Unlike continental and geothermal brines, seawater is abundant and more evenly distributed, and offers a theoretically inexhaustible lithium supply. However, the primary challenge lies in its extremely low lithium concentration alongside very high concentrations of competing ions, particularly sodium and magnesium, which, as seen in Table 2.5, are present at levels several orders of magnitude higher [16]. This creates highly unfavorable selectivity conditions for lithium recovery using conventional techniques. Fortunately, recent advances in separation technologies, such as selective Li insertion/extraction using battery electrode materials, have demonstrated progress in overcoming these limitations [28]. Furthermore, producing clean water via desalination, results in a more concentrated brine as waste. This brine is typically five times more concentrated than the input seawater brine, and approximately 142 million $m^3$ are generated daily [29, 30].

**Table 2.5:** Composition **(mg/L)** of surface seawater and deep sea water [16].

| Water Source | Li | Na | K | Ca | Mg | Sr | B | Mg/Li |
|---|---|---|---|---|---|---|---|---|
| Surface Seawater | 0.17 | 10800 | 392 | 411 | 1290 | 8.1 | 4.45 | 7588 |
| Deep Sea Water | 11.7 | 7240 | 10400 | 39 | 96100 | 0.17 | 320 | 8214 |

### 2.1.5. Battery Leachate

In addition to naturally occurring brines, brines derived from the hydrometallurgical recycling of spent lithium-ion batteries (LIBs) represent a valuable lithium resource. As global battery use scales rapidly, end-of-life LIBs offer an opportunity for circular recovery of lithium and other critical metals, such as cobalt, nickel, and manganese.

Hydrometallurgical recycling processes involve either mechanical pretreatment (e.g., dismantling, crushing, sieving) or thermal treatment (e.g., roasting or smelting), followed by acid leaching to dissolve cathode materials into a metal-rich aqueous solution, often referred to as brine or leachate [31]. The resulting leachate then contains high concentrations of lithium, alongside various transition metals, depending on battery chemistry and leaching conditions.

Table 2.6 summarizes representative metal concentrations in leachates produced using sulfuric acid from various LIB types, illustrating the diversity in ionic composition of synthetic brines.

**Table 2.6:** Metal concentrations **(mg/L)** in leachates from different lithium-ion batteries using sulfuric acid.

| Battery Type | Li | Co | Ni | Al | Fe | Zn | P | F |
|---|---|---|---|---|---|---|---|---|
| $LiCoO_2$ [17] | 5430 | 44720 | – | – | – | – | – | – |
| $LiNiMnCoO_2$ [18] | 3000 | 19000 | 7000 | 600 | 400 | 50 | – | – |
| $LiFePO_4$ [19] | 5465 | – | – | 1999 | 56320 | – | 22785 | 10003 |

These leachates generally do not pose the selectivity challenges for lithium adsorption as natural brines. Most co-dissolved metals are chemically dissimilar to Li in terms of charge density, ionic radius, and hydration energy, making them less competitive for selective adsorption sites. In support of this, a recent study demonstrated that Co adsorption onto lithium ion sieves was negligible compared to Li [32]. Nevertheless, it should be investigated whether the presence of these metals may still affect process performance, for instance, through fouling.

A key challenge, however, is that lithium recovery has not yet been a primary focus in battery recycling. The predominant method used at the industrial scale is pyrometallurgy, which, for recovery of metals such as cobalt, nickel, and copper, offers advantages such as high reaction rates, simplified processing, and the ability to handle large volumes of mixed battery chemistries without preprocessing [33]. However, a significant drawback of pyrometallurgy is that much of the lithium is lost to waste streams (60–70% in the slag and 30–40% in the flue gas) [21, 34]. Despite its higher capital costs, the hydrometallurgical recycling route is predicted to become more profitable than the pyrometallurgical within the next 25 years, considering the trends of decreasing cobalt content in LIBs and increased lithium demand [35].

## 2.2. Lithium Recovery from Brines

As highlighted in section 2.1, brines account for the majority of global lithium production, yet they differ widely in terms of lithium concentration and interfering ions. Developing efficient and robust methods to extract lithium from these sources is vital for meeting increasing demand.

While various separation technologies- including precipitation, solvent extraction, and membrane-based processes- can recover lithium under certain conditions, each comes with trade-offs. Consequently, ion exchange and sorption strategies have garnered increasing attention due to their comparatively high lithium selectivity and stable performance, even with challenging feedstocks [7]. Among these, lithium titanium oxide (LTO) ion sieves have emerged as especially promising, largely due to their robust lattice structure, excellent cyclic stability, and negligible risk of toxic metal dissolution [36, 37]. Two principal LTO sieve variants exist, layered and spinel, both relying on an ion-exchange mechanism wherein $Li^+$ ions selectively re-intercalate into acid-treated vacancies [38, 39].

The following subsections provide an overview of both traditional and emerging lithium recovery techniques for brines (subsection 2.2.1), discuss the evolving field of ion exchange and sorption materials (subsection 2.2.2), and spotlight lithium titanium oxide (LTO) ion sieves (subsection 2.2.3) as a promising approach for selective lithium extraction in high-magnesium environments. This overview aims to contextualize the trade-offs in and future directions of advancing lithium recovery from brines.

### 2.2.1. Overview of Lithium Recovery Techniques

Lithium can be recovered from brine using a variety of techniques, each with its advantages and drawbacks. Four of the most commonly discussed methods include precipitation, solvent extraction, membrane-based processes, and ion exchange/sorption. Below is an overview of these methods.

**Precipitation.** A straightforward and low-cost way to recover lithium from brine is through precipitation, where lithium is converted into a low-solubility compound [40]. This is the most economical method for brines with a Mg/Li ratio below 6 [7]. Brines with higher Mg/Li ratios require preliminary removal of magnesium ions or the use of aluminum compounds to avoid co-precipitation [41]. This approach is relatively simple and cost-effective for high-quality brines, but it can involve chemical additives and high-temperature reactions, both of which are environmentally harmful.

**Solvent Extraction.** Solvent extraction (also known as liquid-liquid or chemical extraction) is a separation technique that uses a biphasic system consisting of an aqueous phase containing lithium ions and an immiscible organic phase with selective extractants [42]. With agitation, the lithium ions migrate to the organic phase due to their chemical affinity. Solvent extraction is suitable for brines with high Mg/Li ratios; however, equipment challenges persist including a large footprint, large liquid volumes, severe corrosion by the extractant, and a long equilibrium time [43].

**Membrane-Based Processes.** A range of membrane-based processes, including nanofiltration and electrodialysis, have attracted attention for lithium recovery due to their moderate (environmental) costs and potential for high selectivity [44]. In nanofiltration, positively charged membranes can allow $Li^+$ passage while rejecting divalent ions. In electrodialysis, an electrical field is applied to a membrane stack which causes the cations to pass through. These membrane operations generally offer good control over separation efficiency and can be combined to create concentrated lithium solutions, but, at a commercial scale, a high Mg/Li ratio in brine remains a challenge for selective recovery and membranes suffer from fouling [41]. Somrani, Hamzaoui, and Pontie, for instance, report a 50% decline in productivity due to fouling after just six hours [45].

**Ion Exchange and Sorption.** Ion exchange and sorption methods have attracted significant attention because they combine high selectivity, even in high-Mg feeds, with comparatively mild operating conditions [7]. Unlike precipitation, which can require complex multi-step approaches for brines with elevated magnesium-to-lithium ratios, or solvent extraction, where handling and regenerating large volumes of organic solvents may increase operational complexity, sorbents often operate efficiently in a broad range of brine chemistries while consuming less chemical input overall [41]. Moreover, membrane-based approaches tend to be prone to fouling, which drives up operational costs [45]. By contrast, ion exchange and sorption methods generally feature simpler setups and have been integrated into continuous processes [7]. For these reasons, ion exchange and sorption materials can be viewed as the most promising route for sustainable lithium recovery.

### 2.2.2. Ion Exchange and Sorption Materials

In lithium recovery, ion exchange and sorption approaches rely on adsorbents or ion-sieves that extract and retain $Li^+$ from brine and subsequently release it into an eluent. Below is an overview of the inorganic and organic sorbents suitable for such applications, followed by a summary of their advantages and drawbacks in Table 2.7.

**Ion-Imprinted Polymers (IIPs).** IIPs are synthetic polymers engineered to contain ion-specific cavities, often incorporating structures like crown ethers or calixarenes [7]. These cavities are tailored to match the size of target ions such as $Li^+$, enabling selective adsorption via size exclusion and chelation, referred to as a lock-and-key model [46]. While IIPs can achieve high adsorption capacities in experiments, industrial application is limited by high production costs and insufficient selectivity in brines with high $Mg^{2+}/Li^+$ ratios [7].

**Lithium–Aluminum Layered Double Hydroxides (LiAl–LDHs).** These materials form through the intercalation of lithium into vacancies in the aluminum hydroxide layers. Their main advantages include stable adsorption and desorption, high selectivity, and simple preparation [7]. Their chief limitations are low lithium adsorption capacity ($\sim 8$ mg $^+$/g) and structural deterioration with repeated use; however, both can be remedied with doping [47, 48, 49].

**Lithium Ion Sieves (LIS).** LIS are considered by some to be the most promising class of materials for lithium recovery from brines, attributed to high separation efficiency, theoretical lithium uptake capacity, cyclic stability, and environmental friendliness [36]. LIS materials are made from lithium-rich precursors, which undergo acid treatment to exchange the lithium for hydrogen ions, creating sites that exhibit high selectivity for lithium ions due to their small size and charge. During the recovery process, lithium ions in the brine are intercalated into these sites via ion exchange. The process is visualized in Figure 2.3.

LISs are categorized based on their chemical composition into two main types: lithium manganese oxide-based (LMO) and lithium titanium oxide-based (LTO) materials. Among these, LMO-LISs are currently the most widely used because of their high lithium uptake capacity and strong lithium selectivity

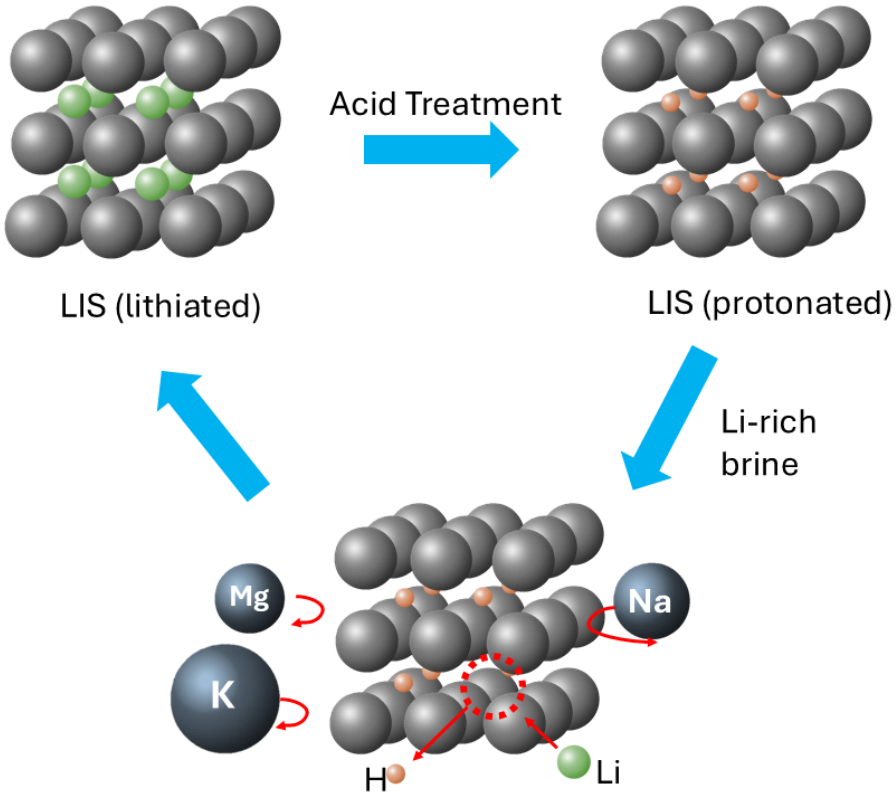


**Figure 2.3:** Schematic representation of the lithium recovery process with lithium ion sieves.

[7, 36]. However, a major drawback of this type is the dissolution of manganese into the aqueous phase, which poses a risk of severe water pollution and reduces cyclic stability [50].

In contrast, LTO-LISs offer a potential solution to this issue, as titanium compounds possess a stronger metal-oxygen bond, making them more resilient to dissolution and, if dissolution occurs, are environmentally benign and can be more easily removed from aqueous solutions [36, 50]. Drawbacks include novelty, slow reaction kinetics (requiring up to a full day to reach equilibrium for both adsorption and desorption), high production costs, and the need for an alkaline brine source to achieve profitable $Li^+$ extraction, as competition between $H^+$ and $Li^+$ for sites increases with acidity [37, 7].

**Table 2.7:** Comparison of major ion exchange and sorption material groups [7].

| Material Group | Advantages | Drawbacks |
|---|---|---|
| **IIPs** | Highly tailored $Li^+$ recognition; achieving high selectivity in synthesized brines | Expensive to produce; struggle with selectivity in real brines with excessive $Mg^{2+}$ |
| **LiAl–LDHs** | Proven column operations; high $Li^+$ selectivity | Lower capacity ($\sim$ 8 mg/g); risk of structural collapse if over-desorbed |
| **LMO–LISs** | Higher $Li^+$ uptake ($\sim$ 30 mg/g); strong $Mg^{2+}$ discrimination | Manganese dissolution in acid; doping/coating adding cost and complexity |
| **LTO–LISs** | Robust lattice and minimal dissolution; capacity $\sim$ 30 mg/g; performs well at high $Mg^{2+}$ | Typically requiring mild alkaline conditions; high synthesis cost; slow |

Collectively, LTO-LISs hold a unique advantage for large-scale processing of challenging brines. Their balance of capacity, stability, and regenerative ability has brought them to the forefront of emerging lithium recovery solutions.

### 2.2.3. Lithium Titanium Oxide Lithium-ion Sieves for Lithium Recovery

Lithium titanium oxide lithium-ion sieves (LTO-LISs) have emerged as a promising technology for extracting lithium from brines and seawater due to their high selectivity and structural stability [36]. Generally, two classifications exist based on crystal structure: layered ($Li_2TiO_3$) and spinel ($Li_4Ti_5O_{12}$) [37].

Layered $Li_2TiO_3$ has a monoclinic structure, with alternating $TiO_6$ octahedra and lithium layers. Spinel $Li_4Ti_5O_{12}$ has a cubic structure, forming a three-dimensional network of $TiO_6$ octahedra, instead of flat layers [7]. Both structures are visualized in Figure 2.4. In the layered structure, lithium occupies two types of sites: about 75% of Li resides in pure (Li) layers, while the remaining $\sim$25% is located in mixed ($LiTi_2$) layers, where one-third of the positions are filled by Li and two-thirds by Ti. In contrast, the spinel structure distributes lithium more symmetrically: $Li^+$ ions occupy the tetrahedral 8a sites and one-sixth of the octahedral 16d sites, while the remaining 16d sites are filled by $Ti^{4+}$. The layered material typically offers a higher theoretical lithium uptake capacity; however, the spinel material has demonstrated superior lithium selectivity, chemical stability, and cyclical stability with repeated adsorption/elution cycles [7, 37].

As mentioned in subsection 2.2.2, acid treatment exchanges the lithium from these structures, forming $H_4Ti_5O_{12}$ and $H_2TiO_3$, which selectively re-insert $Li^+$ in repeated adsorption–desorption cycles, as shown in Figure 2.3. Even in brines where lithium is outnumbered by several orders of magnitude, LTO sieves consistently demonstrate a strong preference for $Li^+$ [37]. This selectivity stems from the compatibility of lithium with the original lattice sites, making it energetically favorable for $Li^+$ to re-insert. Wei et al. quantify this experimentally for the spinel structure with results shown in Table 2.8.

**Table 2.8:** Adsorption selectivity of $Li_4Ti_5O_{12}$ nanofibers, demonstrating high selectivity for lithium ions [52].

| Parameter | ($Li^+$) | ($K^+$) | ($Na^+$) | ($Mg^{2+}$) | ($Ca^{2+}$) |
|---|---|---|---|---|---|
| Initial concentration (mg/L) | 40 | 443 | 241 | 501 | 535 |
| Adsorption capacity at equilibrium (mg/g) | 7.58 | 0.52 | 0.34 | 0.44 | 0.31 |
| Distribution coefficient (mL/g) | 232 | 1.17 | 1.41 | 0.88 | 0.58 |
| Relative selectivity factor | 1 | 197 | 165 | 264 | 400 |

Several approaches have emerged to address the inherent limitations of LTO, such as slow adsorption and the need for high-pH environments, as well as to improve selectivity and uptake capacity. Key

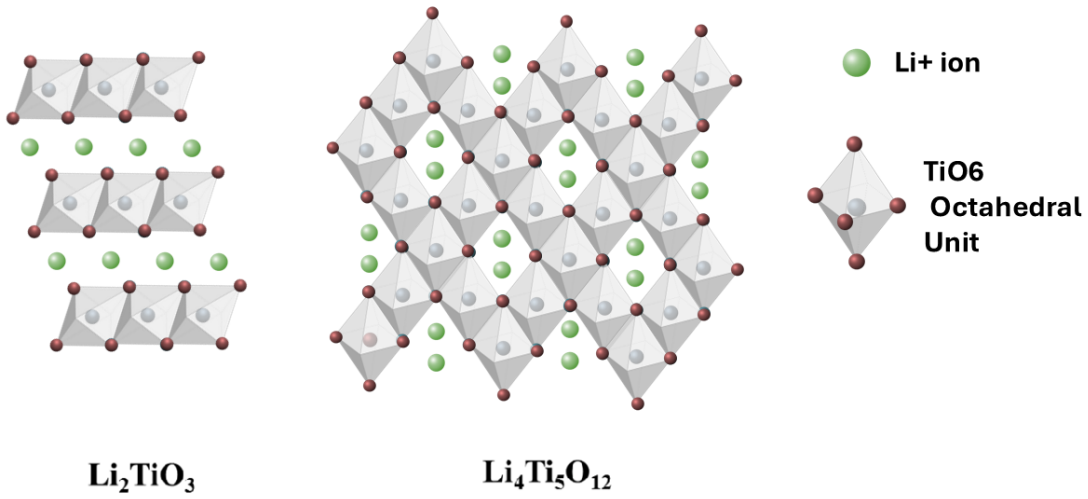


**Figure 2.4:** Comparison of spinel and layered Lithium Titanium Oxides [51]. Lithium in the Ti-sublattice octahedra is not shown.

advancements can be summarized as follows:

**Material Doping.** One of the most promising strategies involves elemental doping to enhance performance, often through the reduction of particle aggregation [53, 39]. For example, Zhou et al. demonstrate that Zr-doped layered LTO exhibits a significantly improved lithium adsorption capacity, up to 93.2 mg $g^{-1}$, representing a 65.5% increase over undoped LTO [39]. Other dopants, including Mo, Fe, and Ni, have also shown improvements for the layered structure regarding adsorption capacity, magnetic separation efficiency, structural stability, hydrophilicity, and lithium selectivity [53, 54, 38, 55]. For the spinel structure, Zheng et al. demonstrate that doping with $La^{3+}$ cations improved adsorption performance by stabilizing the crystal structure, reducing particle agglomeration, expanding the lithium-ion channels, and decreasing resistance to lithium-ion migration [56].

**Structural Design.** Efforts have been made to modify the structure of LTO to improve adsorption kinetics. These modifications primarily aim to increase the material's surface area, which exposes more adsorption sites, by tailoring its morphology into forms such as nanotubes, nanowires, nanosheets, nanorods, porous microspheres, and nanoparticles [57]. For instance, yolk-shell architectures (spheres with a carbon center and a spinel LTO shell with a hollow space in between), were shown by Li et al. to accelerate adsorption speed and enhance the LTO sieve capacity [58]. Nanospheres assembled by Li et al. even reach adsorption equilibrium within one hour. Pu et al. also managed to improve the equilibrium time by introducing lattice defects, particularly oxygen vacancies, which reduce the internal mass transfer resistance [60].

**Sustainable and Cost-Effective Production.** To reduce the cost and environmental footprint of LTO synthesis, alternative raw materials such as titania slag, sewage sludge, and other industrial waste streams have been evaluated as titanium sources [7].

While LTO sieves hold considerable promise for lithium recovery from brines, limitations such as slow ion-exchange kinetics, high preparation cost, and challenges in process scalability remain [7]. In addition to addressing these engineering barriers, future research should also focus on deepening the fundamental understanding of ion-exchange mechanisms in spinel-structured LTO materials. Although recent studies have demonstrated that crystal facet orientation significantly influences lithium adsorption and desorption performance, underlying ion-exchange mechanisms in spinel structures remain underexplored at the atomic level [61, 62]. This gap motivates the present study, which investigates spinel LTO using computational methods. In contrast, layered LTO has been more extensively studied by Lu et al. using DFT calculations, revealing detailed ion-exchange energetics and site-specific pathways [11]. Moreover, layered structures seem to have seen more progress in doping strategies to

improve performance, whereas such modifications remain less explored in spinel systems. Additionally, future work should prioritize improving performance not only in alkaline brines but also in acidic and neutral brines.

## 2.3. Computational Methods for Investigating Lithium Recovery

As highlighted in subsection 2.2.3, lithium titanium oxide (LTO) ion-sieve materials hold considerable potential for sustainable and efficient lithium extraction, yet still exhibit several performance shortcomings. These include slow ion-exchange kinetics and limited adsorption capacity in acidic operating conditions. Improving the composition and structure of LTO materials can address these challenges, but experimental optimization is often costly and time-consuming.

Computational methods offer a more efficient route by illuminating the mechanisms that govern lithium selectivity. Such methods create insight into atomic-scale factors that directly influence the adsorption process. This way, informed adjustments, such as with doping, can be made.

This subsection explains the principles behind quantum-mechanical modeling. It also summarizes relevant computational work on lithium-ion sieves. By highlighting how computational studies have created knowledge for similar materials, the account hopes to provide a framework for how spinel LTO may be approached for improvement.

### 2.3.1. Quantum Mechanical Approach

Quantum mechanical methods are essential to investigate lithium recovery mechanisms at the atomic scale, as they allow for a fundamental understanding of how lithium ions interact with host materials. This subsection follows the explanation of Density Functional Theory (DFT) given by Sholl and Steckel [63]. In DFT the foundation lies in the time-independent Schrödinger equation, which describes the energy and behavior of electrons in a material:

$$\hat{H}\Psi = E\Psi \tag{2.1}$$

Here, $\hat{H}$ is the Hamiltonian operator, $\Psi$ is the many-electron wavefunction, and $E$ is the total energy of the system. The Hamiltonian comprises several terms representing the kinetic energy of electrons, their interactions with atomic nuclei, and electron–electron interactions:

$$\hat{H} = -\frac{h^2}{2m}\sum_{i=1}^{N}\nabla_i^2 + \sum_{i=1}^{N}V(\mathbf{r}_i) + \sum_{i=1}^{N}\sum_{i<j}^{N}U(\mathbf{r}_i,\mathbf{r}_j) \tag{2.2}$$

Solving this equation exactly becomes infeasible for systems with many electrons, as the wavefunction $\Psi$ depends on $3N$ spatial variables for $N$ electrons. DFT resolves this by replacing the wavefunction with the electron density $n(\mathbf{r})$, a function of only three spatial coordinates.

According to the first Hohenberg–Kohn theorem, the ground-state energy of an electron system is a unique functional of its electron density:

$$E[n(\mathbf{r})] \tag{2.3}$$

The second Hohenberg–Kohn theorem establishes that the electron density that minimizes this energy functional corresponds to the true ground-state density. However, the exact form of this energy functional is unknown. Kohn and Sham introduced a practical approach by expressing the total energy as a sum of known and unknown contributions:

$$E[n(\mathbf{r})] = T[n] + E_{\mathsf{ext}}[n] + E_{\mathsf{H}}[n] + E_{\mathsf{XC}}[n] \tag{2.4}$$

Here $T[n]$ is the kinetic energy of non-interacting electrons, $E_{\mathsf{ext}}[n]$ is the energy from the external potential (nuclei), $E_{\mathsf{H}}[n]$ is the electrostatic (Hartree) energy, and $E_{\mathsf{XC}}[n]$ is the exchange–correlation energy.

The Kohn–Sham equations, derived from minimizing this total energy, are:

$$\left[-\frac{\hbar^2}{2m}\nabla^2 + V_{\text{ext}}(\mathbf{r}) + V_{\text{H}}(\mathbf{r}) + V_{\text{XC}}(\mathbf{r})\right]\psi_i(\mathbf{r}) = \varepsilon_i\psi_i(\mathbf{r}) \tag{2.5}$$

Here $\psi_i(\mathbf{r})$ are the single-electron orbitals, $V_{\text{H}}(\mathbf{r}) = \int \frac{n(\mathbf{r}')}{|\mathbf{r}-\mathbf{r}'|}\,d\mathbf{r}'$ is the Hartree potential, and $V_{\text{XC}}(\mathbf{r}) = \delta E_{\text{XC}}/\delta n(\mathbf{r})$ is the exchange–correlation potential.

To solve these equations in practice, one encounters an apparent circularity: the Kohn–Sham equations require the electron density $n(\mathbf{r})$ to construct the Hartree and exchange–correlation potentials, yet the density itself is obtained from the orbitals $\psi_i(\mathbf{r})$ that result from solving these equations. This problem is resolved through an iterative self-consistent procedure (visualized in Figure 2.5):

1. Begin with an initial guess for the electron density $n(\mathbf{r})$.
2. Construct the effective potentials $V_{\text{ext}}(\mathbf{r})$, $V_{\text{H}}(\mathbf{r})$, and $V_{\text{XC}}(\mathbf{r})$.
3. Solve the Kohn–Sham equations to obtain the orbitals $\psi_i(\mathbf{r})$.
4. Recompute the electron density from these orbitals:

$$n(\mathbf{r}) = 2\sum_i |\psi_i(\mathbf{r})|^2 \tag{2.6}$$

   where the factor of 2 accounts for spin.
5. Compare the new density with the previous one. If they differ, update the guess and repeat until the input and output densities agree within a chosen tolerance.

This self-consistent field (SCF) cycle yields the ground-state density and total energy of the system once convergence is reached. The remaining challenge lies in approximating the exchange–correlation functional $E_{\text{XC}}[n]$. This functional accounts for quantum mechanical effects of electron-electron interactions, specifically, how electrons avoid each other due to their charge and the Pauli exclusion principle. The simplest approach is the *Local Density Approximation* (LDA), which assumes the exchange–correlation energy at each point in space is the same as that of a uniform electron gas with the same local density. More advanced approximations, such as the *Generalized Gradient Approximation* (GGA), incorporate not only the local density but also its gradients to improve accuracy. These approximations allow DFT to provide a practical balance between computational efficiency and predictive accuracy.

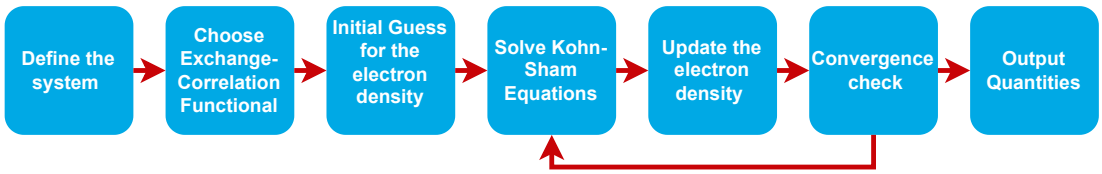


**Figure 2.5:** Workflow of a DFT calculation.

Several computational packages are available to perform DFT calculations, each offering strengths depending on the application. VASP (Vienna Ab initio Simulation Package) is a widely used commercial code for DFT. It employs plane-wave basis sets and efficient pseudopotential methods, making it highly accurate for solids [64]. Quantum ESPRESSO is a similar open-source code, also based on plane-wave DFT and pseudopotentials [65]. GPAW is a Python-based DFT code that implements the projector-augmented wave (PAW) method and is highly suitable for high-throughput simulations [66]. CASTEP is particularly known for its strong support for spectroscopy-related calculations providing direct links between theory and experiment [67]. FHI-aims is an all-electron code based on numeric atom-centered orbitals making it well-suited for high-precision simulations of complex materials [68]. SIESTA uses a localized atomic orbital basis set and norm-conserving pseudopotentials to enable efficient DFT calculations. It is particularly effective for large systems due to its linear-scaling capabilities and tunable accuracy-cost tradeoff [69].

### 2.3.2. Computational Studies for Lithium-Ion Sieve Materials

Despite the promise of spinel lithium titanate (LTO) as a lithium-ion sieve, challenges such as sluggish ion-exchange kinetics hinder its practical application. To address this limitation with computational modeling, it may be beneficial to draw insights from computational studies on related materials. This section highlights key findings from DFT simulations applied to spinel lithium manganese oxide (LMO) and layered LTO. These materials share similarities to spinel LTO, some of which are evident in their crystal structures shown in Figure 2.6. Although these are not direct analogs, they may provide valuable information on lithium site preferences and diffusion barriers relevant to spinel LTO. These insights serve as a starting point for guiding potential performance improvements in spinel LTO sieves.

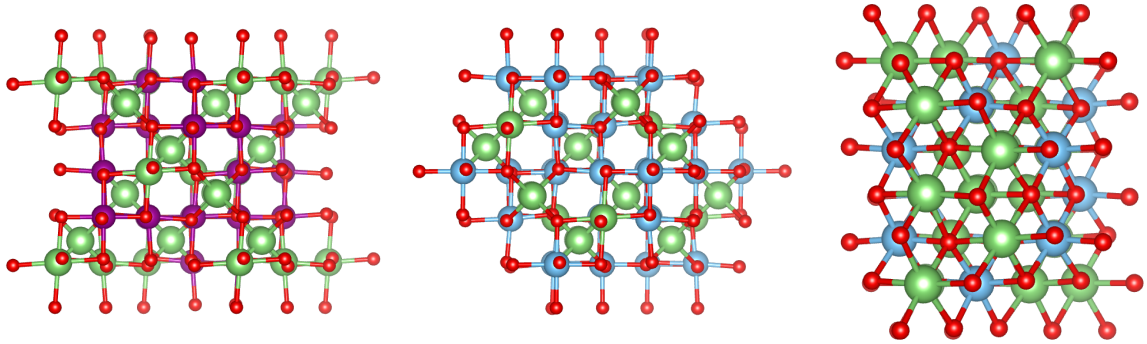

(a) (b) (c)

**Figure 2.6:** Crystal structures of different lithium-ion sieves: (a) $Li_4Mn_5O_{12}$, (b) $Li_4Ti_5O_{12}$, and (c) $Li_2TiO_3$.

#### Spinel Lithium Manganese Oxide

In a study by Gao et al. on spinel lithium manganese oxides (LMO), DFT was used to investigate lithium desorption mechanisms [70]. The results revealed that lithium ions occupying the 8a tetrahedral sites exhibited lower reaction and diffusion energy barriers than those at the 16d octahedral sites. Moreover, lithium diffusion favors shorter, energetically accessible pathways between nearby 8a sites, while migration into or through 16d sites was associated with higher energy barriers. This could mean that to optimize for lithium adsorption, strategies should focus on increasing the proportion of $Li^+$ in 8a sites.

Xu and Meng show that using generalized gradient approximation (GGA) as an exchange correlation functional fails to distinguish between $Mn^{3+}$ and $Mn^{4+}$ ions in DFT modeling of spinel LMO [10]. By incorporating a Hubbard U correction, a GGA+U method enables correct charge separation and reveals how the local $Mn^{3+}/Mn^{4+}$ configuration directly impacts lithium diffusion. This exchange correlation was also used by Gao et al. [70]. Xu and Meng find that lithium ions migrate through the lattice by hopping from one tetrahedral 8a site to another via intermediate 16c octahedral sites, and the energy barrier for this diffusion step is sensitive to the charge and spatial arrangement of the Mn ions [10].

The study showed that diffusion barriers are significantly reduced when the 16c site is surrounded by more $Mn^{4+}$ ions instead of $Mn^{3+}$. This explains why doping spinel LMO with elements like $Ni^{2+}$, $Cu^{2+}$, or $Co^{2+}$, which increase the $Mn^{4+}$ fraction, has been shown to improve lithium mobility.

Zhang et al. propose a strategy of both doping and surface coating to reduce Mn dissolution and improve the structural integrity of LMO sieves [71]. DFT calculations were used to explore the mechanism behind a lithium lanthanum titanate (LLTO) surface coating and Ti/La doping. Six crystal structures were modeled to represent various doping strategies: Ti interstitial, La interstitial, Ti substitutional at Mn sites, La substitutional at Mn sites, co-doping of Ti and La (1:1), and co-doping with a higher Ti:La ratio. The calculated formation energies for these models were 0.15, −0.28, −2.19, −4.24, −7.56, and −7.89 eV, respectively. The most favorable configuration corresponds to substitutional co-doping at Mn sites with a Ti-rich ratio, indicating enhanced structural stability. Additional results showed that the modification suppresses side reactions (dissolution) and promotes Li-ion transport.

### Layered Lithium Titanium Oxide

Lu et al. used DFT calculations and experiments to study how lithium ions are adsorbed by $H_2TiO_3$ [11]. Three distinct ion-exchange pathways were identified within the layered structure: Li1–H1, Li2–H2, and Li3–H3. The calculated adsorption energies for these pathways were all negative, indicating that exchange is thermodynamically favorable. Among them, the Li3–H3 pathway exhibited the most favorable adsorption energy (−7.270 eV), followed by Li2–H2 (−6.761 eV) and Li1–H1 (−6.656 eV), establishing a clear order of preferential ion exchange. Additionally, lithium migration energy barriers were assessed, showing that migration into Li3–H3 sites from Li1–H1 or Li2–H2 requires less energy, whereas reverse or lateral migration is associated with higher barriers.

The structural differences between $Li_2TiO_3$ and $H_2TiO_3$ were also analyzed. After lithium removal, the formation of strong H–O bonds leads to significant structural changes. For instance, H1–O1 bond lengths were calculated to be 0.974 Å, considerably shorter than the Li1–O1 bonds at 2.077 Å. These stronger H–O bonds introduce distortion in the layered structure and increase the energy barrier for re-adsorption of $Li^+$ ions, limiting lithium uptake.

In a study by Liu et al. DFT calculations were used to evaluate the binding energies and most stable lithium adsorption sites (Li layer or $LiTi_2$ layer) across four structural models of $Li_2TiO_3$ and $H_2TiO_3$ [72]. The results showed that $Li_2TiO_3$ configurations yielded positive binding energies, indicating a poor driving force for lithium adsorption. In contrast, $H_2TiO_3$ exhibited negative binding energies, with the most stable configuration corresponding to lithium adsorption in the Li layer ($\Delta E = -3.12$ eV). These findings indicate that lithium ions preferentially adsorb between the layers of the $H_2TiO_3$ structure.

Chen conducted simulations to investigate lithium adsorption thermodynamics, phase transitions, and structural changes in pure $H_2TiO_3$, Mo-doped, and Fe-doped variants, revealing a two-phase behavior in all structures [73]. For the pure and Fe-doped systems, a phase transition was identified between a Li-poor and Li-rich phase around Li $\sim$80 mg $g^{-1}$. Mo-doped systems exhibited a more gradual transition due to the structural flexibility created by the larger Mo atoms.

Volume and lattice constant changed with phase transitions, showing expansion followed by contraction in the vertical direction and continuous shrinkage in the lateral direction with increasing lithium content.

Three distinct lithium configurations were identified. In the Li-rich phase, Li atoms predominantly occupied the Ti and central layer sites. In the Li-poor phase, two sub-phases were identified: (I) at very low Li loading, with Li in the Ti layer, and (II) at slightly higher loading, with Li primarily in the central layer. The Li-poor (I) to Li-poor (II) transition occurs around 35 mg $g^{-1}$.

# 3

# Methodology

The present study will use DFT simulations to investigate the intercalation behavior and thermodynamic stability of spinel lithium titanium oxide (LTO) under lithium extraction and proton exchange. Calculations were performed using the Vienna Ab initio Simulation Package (VASP). The projector-augmented wave (PAW) method was used to describe the interaction between core and valence electrons, and the exchange-correlation functional was treated within the generalized gradient approximation (GGA) using the Perdew–Burke–Ernzerhof (PBE) parameterization.

Convex hull analysis across three transformation types ensures that the full energetic landscape is mapped accurately, allowing for the identification of thermodynamically preferred compositions. However, thermodynamic favorability alone does not capture the kinetic feasibility of transitions between these states. To address this, the Nudged Elastic Band (NEB) method will be employed to investigate diffusion pathways and activation energy barriers for configurations that lie on the convex hull. In this way, NEB complements the convex hull analysis by identifying which lithium or proton migration processes are not only energetically favorable but also kinetically accessible. Together, these techniques provide a picture of both stability and mobility in the LTO system.

## 3.1. Density Functional Theory Preparation

Before performing these simulations, the computational parameters and delithiation site preferences must be validated to ensure a reliable calculation.

### 3.1.1. Brillouin Zone Division Convergence

The KPOINTS file tells VASP how the calculation is divided over the Fourier transform of a crystal's real-space lattice, also known as the Brillouin Zone. A denser $k$-point mesh increases accuracy, but also may increase the time necessary for convergence. A convergence test, therefore, starts with a coarse mesh and adds more $k$-points until the change in total energy falls below a target 1% [63]. Calculations for $Li_4Ti_5O_{12}$ were performed using four Monkhorst–Pack meshes, listed in Table 3.1 along with their calculated energies.

**Table 3.1:** Total energy of $Li_4Ti_5O_{12}$ as a function of $k$-point mesh.

| Mesh | $E_0$ (eV) |
|---|---|
| 2 × 2 × 2 | –875.93267 |
| 3 × 3 × 3 | –875.92876 |
| 4 × 4 × 4 | –875.93162 |
| 5 × 5 × 5 | –875.93119 |

The spread of the energies is 3.91 meV, which is far below the 1% threshold. The 2 × 2 × 2 grid, therefore, provides sufficient accuracy and is used for all further calculations.

### 3.1.2. Input Settings and Validation via Voltage Comparison

The INCAR file controls critical simulation parameters such as the energy cutoff, electronic convergence criteria, smearing method, and whether spin polarization is considered. These settings, listed in Table 3.2, directly affect total energy values and, by extension, the computed voltages.

**Table 3.2:** INCAR tags used for $Li_4Ti_5O_{12}$ calculations.

| Tag | Value |
|---|---|
| ENCUT | 520 eV |
| PREC | ACCURATE |
| ISMEAR | 1 |
| NELM / NELMIN | 120 / 5 |
| IBRION | 2 |
| NSW | 1000 |
| ISIF | 3 |
| LREAL | Auto |
| LASPH | .TRUE. |
| ISYM | 0 |
| ISPIN | 2 |
| NPAR | 4 |
| LWAVE / LCHARG | .FALSE. / .FALSE. |

The implications of these tags are explained by VASP wiki as follows [74]:

- **ENCUT = 520 eV.** The energy cutoff (`ENCUT`) sets the maximum kinetic energy of the plane-wave basis. It should be higher than the `ENMAX` value from the POTCAR file, which is the recommended minimum for accurate results. For oxygen, `ENMAX` is 400 eV. A factor of 1.3 was applied to ensure convergence, resulting in a final cutoff of 520 eV. Higher values can improve accuracy further but increase the computational cost.
- **PREC = ACCURATE.** This tag sets the precision level for the calculation. It controls the density of the discrete grid used to represent charge densities and potentials in real space. This is especially important in PAW calculations, where core electrons are treated implicitly to save computational cost. The `ACCURATE` setting increases grid density and sets a default `ENCUT` to approximately 1.3 times the default value defined in the POTCAR, improving the reliability of forces and stress calculations. However, it also increases memory usage and computation time.
- **ISMEAR = 1.** This setting controls how electrons are distributed near the Fermi level—the highest occupied energy level at absolute zero. Without smearing, electrons are assigned sharply: energy states are either fully occupied or completely empty. In systems with energy levels very close to the Fermi level, this can cause the total energy to change abruptly between self-consistent steps, making the calculation slow to converge. `ISMEAR = 1`, typically suitable for metals, uses Methfessel–Paxton smearing to smooth the transition between occupied and unoccupied states. This improves numerical stability and helps the electronic structure converge more reliably. It is well-suited for spinel LTO, where the presence of one $Ti^{3+}$ ion introduces partially filled $d$-orbitals and thereby a metallic character.
- **NELM = 120, NELMIN = 5.** These tags control the number of electronic steps in each self-consistent step. `NELM` sets the maximum number of steps, and `NELMIN` ensures that a minimum number of steps is performed before checking for convergence. A high value of `NELM` (120) provides enough room for convergence in more challenging systems, while a minimum of 5 steps (`NELMIN = 5`) helps prevent premature convergence due to numerical noise.
- **IBRION = 2.** This tag determines how the atomic positions (and, if allowed, the cell) are updated during structural relaxation. `IBRION = 2` uses the conjugate gradient algorithm—an iterative optimization method that starts with an initial guess, calculates the forces on each atom, and moves the structure toward lower energy. Unlike simpler methods, conjugate gradient takes into account

the direction of previous steps, helping to avoid inefficient zigzagging. It works particularly well when combined with `ISIF = 3`.

- **NSW = 1000.** This tag sets the maximum number of ionic steps allowed during structural relaxation. In each step, the atomic positions are updated based on the calculated forces. Setting a high enough limit ensures that the system has enough steps to fully relax. However, it is also important to define a limit to avoid getting stuck in unconverged states.
- **ISIF = 3.** This tag controls how the stress tensor is calculated and which parts of the structure are allowed to relax during ionic optimization. `ISIF = 3` enables full relaxation, allowing the atomic positions, cell shape, and cell volume to change. This is the only setting that permits completely unconstrained relaxation, making it necessary when the equilibrium structure is unknown.
- **LREAL = Auto.** This tag determines whether the projection is carried out in real space or reciprocal space. Electrons are wave-like, and their properties are more naturally described in reciprocal (Fourier) space. However, performing projections in reciprocal space is computationally more expensive. Real-space projection is faster and typically sufficient for large systems (more than 100 atoms), while reciprocal-space projection offers slightly higher accuracy for smaller systems. The `Auto` setting allows VASP to choose the projection method based on system size
- **LASPH = .TRUE.** This tag determines whether non-spherical contributions to the gradient of the electron density are included. These contributions come from the shape of atomic orbitals—especially $d$- and $f$-orbitals, which are not spherically symmetric. Including these effects is necessary for systems with transition metals like Ti. Enabling `LASPH` improves the reliability of the results, but increases the computational cost.
- **ISYM = 0.** This tag controls how symmetry is handled in the calculation. Setting `ISYM = 0` disables all symmetry operations. While keeping symmetry on can speed up the calculation by reducing the number of atoms and operations, it may also artificially constrain the system by preventing it from experiencing distortions or phase transitions.
- **ISPIN = 2.** This tag specifies whether spin polarization is included in the calculation. `ISPIN = 2` enables spin-polarized calculations, where spin-up and spin-down electrons are treated separately. This is needed for systems that may exhibit magnetic behavior; in spinel LTO, the presence of a $Ti^{3+}$ ion introduces a single unpaired electron in the $d$-orbitals, making spin polarization necessary.
- **NPAR = 4.** This tag sets the number of electronic bands that are treated in parallel during the calculation. Increasing `NPAR` can improve computational efficiency by distributing the workload across multiple processor cores. The optimal value depends on the system size and available hardware.
- **LWAVE = .FALSE., LCHARG = .FALSE.** These tags control whether the wave functions and charge densities are written to the output files `WAVECAR` and `CHGCAR`, respectively, at the end of the calculation. Setting them to `.FALSE.` saves disk space when these files are not needed. If set to `.TRUE.`, the saved wave functions and charge densities can be reused in future calculations.

To validate these computational choices and selected level of theory for spinel LTO, a lithium insertion reaction will be simulated:

$$Li_4Ti_5O_{12} \rightarrow Li_7Ti_5O_{12} \tag{3.1}$$

This transformation, seen in Figure 3.1, is experimentally and computationally well-characterized, with a reported voltage plateau of 1.55 V versus $Li/Li^+$ [75, 76].

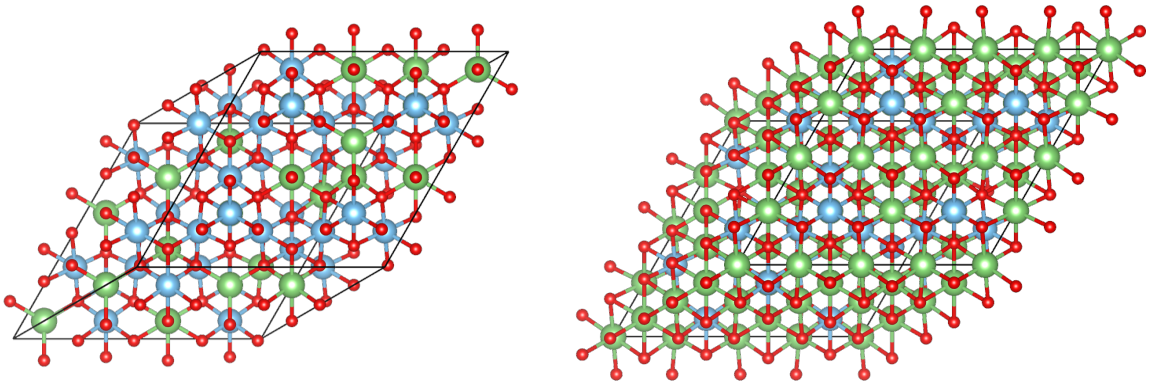


**Figure 3.1:** Crystal structures of (a) $Li_4Ti_5O_{12}$ and (b) $Li_7Ti_5O_{12}$.

The average voltage can be derived from total energy differences using [77]:

$$\bar{V} = \frac{-\left[E_{\mathrm{Li}_x\mathrm{Host}} - (x-y)E_{\mathrm{Li}} - E_{\mathrm{Li}_y\mathrm{Host}}\right]}{(x-y)e} \tag{3.2}$$

Here, $E_{\mathrm{Li}_x\mathrm{Host}}$ and $E_{\mathrm{Li}_y\mathrm{Host}}$ are the DFT total energies of the host material with $x$ and $y$ lithium atoms, respectively. $E_{\mathrm{Li}}$ is the energy per atom of bulk lithium metal, and $e$ is the elementary charge. The values of $x$ and $y$ are determined from the convex-hull plot (Figure 3.2), which is constructed by calculating the formation enthalpy for the lowest energy compositions of $\mathrm{Li}_n\mathrm{Ti}_5\mathrm{O}_{12}$ with several values from $n = 21$ to $37$. The formation enthalpy at each composition is evaluated relative to the endpoints $n_{min} = 21$ and $n_{max} = 37$, using the expression:

$$\Delta H_{\mathrm{f}}(n) = E_{\mathrm{Li}_n\mathrm{Host}} - \left[z\, E_{\mathrm{Li}_{n_{max}}\mathrm{Host}} + (1-z)\, E_{\mathrm{Li}_{n_{min}}\mathrm{Host}}\right], \qquad z = \frac{n - n_{min}}{n_{max} - n_{min}}. \tag{3.3}$$

The lower edge of this plot (the convex line) identifies the most thermodynamically stable compositions. In this case, seen in Figure 3.2, all intermediate formation enthalpies are positive, indicating that only $Li_{21}$ and $Li_{37}$ lie on the convex hull. Therefore, $y = 21$ and $x = 37$ are used in the voltage calculation with Equation 3.2. If any intermediate composition had a negative formation enthalpy, those points would instead define $x$ and $y$.

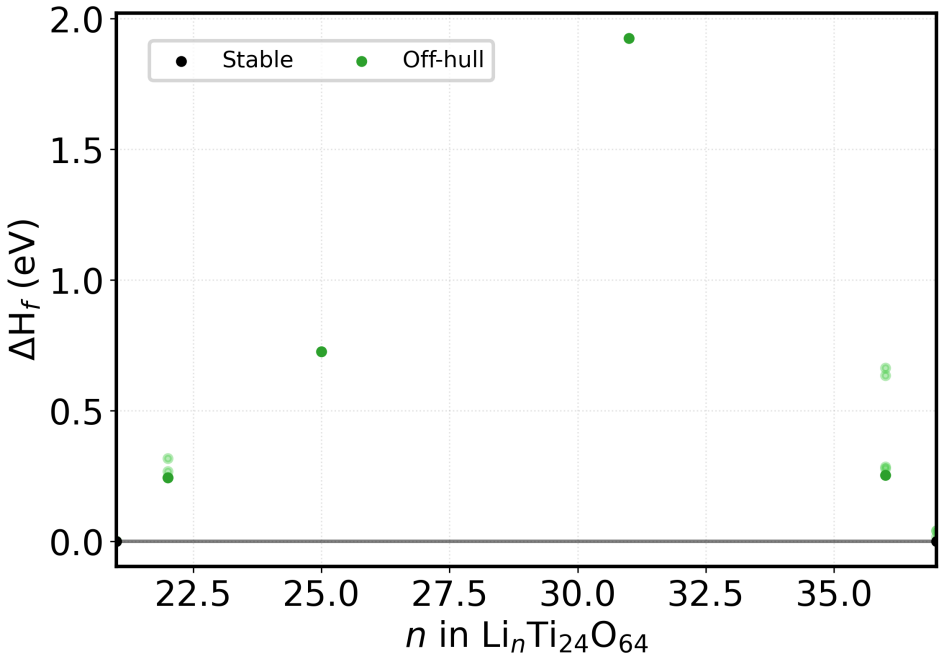


**Figure 3.2:** Formation-enthalpy diagram for lithium insertion cycle $Li_nTi_{24}O_{64}$ ($n = 21, 22, 25, 31, 36, 37$). Only the end-members lie on the lower convex line indicating a phase-separating reaction pathway.

Using the total energies obtained from DFT, the average insertion voltage between $Li_{21}Ti_5O_{12}$ and $Li_{37}Ti_5O_{12}$ was calculated to be 1.44 V. This value falls above the range reported in previous first-principles studies. For example, Sarantuya et al. obtained average voltages of 1.4 V using GGA and 1.3 V using GGA+$U + J_0$ [75]. These values were considered sufficiently accurate for modeling lithium intercalation in spinel LTO. Since the present result of 1.44 V is in even closer agreement with the experimentally observed voltage of 1.55 V [75, 76], it can be concluded that the current INCAR settings are adequate for describing the behavior of $Li_4Ti_5O_{12}$.

### 3.1.3. Delithiation Site Preference Test

Before generating trial structures, a test was performed to determine whether lithium should be taken first from the tetrahedral 8a sites or from the octahedral 16d sites, or whether removal could be left at random. Eight supercells were built and relaxed:

- Near-empty spinel ($Li_{0.2}Ti_5O_{12}$): One Li or one H was kept on either an 8$a$ or a 16$d$ position, giving four structures in total.
- Near-full spinel ($Li_{3.8}Ti_5O_{12}$): All lithium sites were filled by Li except for either a single vacancy or an H on 8a or 16d, again giving four structures.

The DFT energies obtained for these eight cells are listed in Table 3.3. The widest gap between any pair of Li-containing models is $\sim 3.9$ eV for the whole 112-atom supercell, which converts to less than $36$ meV per atom.

As the energy differences are below the accuracy target of the study, neither crystallographic site shows a clear thermodynamic preference for the first lithium atom that leaves the lattice. With this in mind, and to preserve an unbiased thermodynamic perspective, lithium vacancies are allowed to form on 8a and 16d positions at random.

**Table 3.3:** DFT energies of the eight site-preference test cells.

| Configuration | $E_0$ (eV) |
|---|---|
| $H_{0.2}(8a)Ti_5O_{12}$ | $-734.7746$ |
| $H_{0.2}(16d)Ti_5O_{12}$ | $-734.2445$ |
| $Li_{0.2}(8a)Ti_5O_{12}$ | $-736.0823$ |
| $Li_{0.2}(16d)Ti_5O_{12}$ | $-735.1256$ |
| $H_{0.2}Li_{3.8}(8a)Ti_5O_{12}$ | $-875.1611$ |
| $H_{0.2}Li_{3.8}(16d)Ti_5O_{12}$ | $-873.1145$ |
| $Li_{3.8}(8a)Ti_5O_{12}$ | $-871.2243$ |
| $Li_{3.8}(16d)Ti_5O_{12}$ | $-871.6717$ |

## 3.2. Convex Hull Constructions

A similar approach to that described in subsection 3.1.2 is applied to the creation of a convex hull for the delithiation process:

$$Li_4Ti_5O_{12} \rightarrow Li_{4-x}Ti_5O_{12}, \quad 0 \leq x < 4 \tag{3.4}$$

The full delithiation transformation is visualized in Figure 3.3.

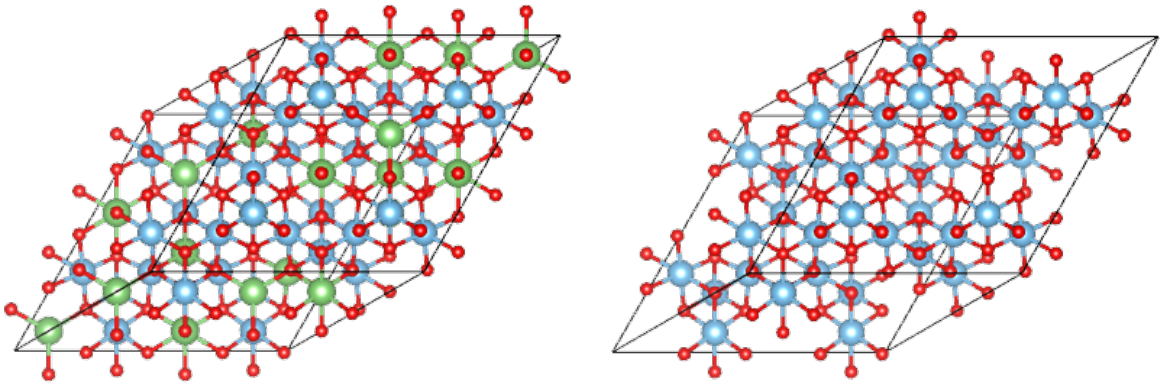

(a) (b)

**Figure 3.3:** Unrelaxed crystal structures of (a) spinel LTO and (b) fully delithiated spinel LTO.

At each lithium removal step, 100,000 trial structures were generated by removing the required number of Li atoms at random from the supercell, which contains 21 Li sites. For every trial, the sum of all Li–Li distances was determined. While the ten trials with the largest total Li–Li distance were kept to represent the pristine state, one trial with an intermediate distance sum (cycled–intermediate) and one with the smallest distance sum (cycled–clustered) were also included. The terms ”pristine” and ”cycled” are used here for consistency with Liu et al., who attributed discrepancies between experimental and computed voltage profiles to cycling effects, namely, the tendency of lithium atoms not to fully resettle into their energetically favorable, well-dispersed positions after repeated use [76]. As in that Li-insertion study, the pristine variants are expected to exhibit greater stability during delithiation. Here, cycled variants are also included to test this assumption. Therefore, for each delithiation step, twelve structures (ten pristine, one cycled-intermediate, and one cycled-clustered) were sent to the DFT calculation to build the convex hull. Differences in the spread of Li atoms between pristine and cycled configurations can be seen in Figure 3.4.

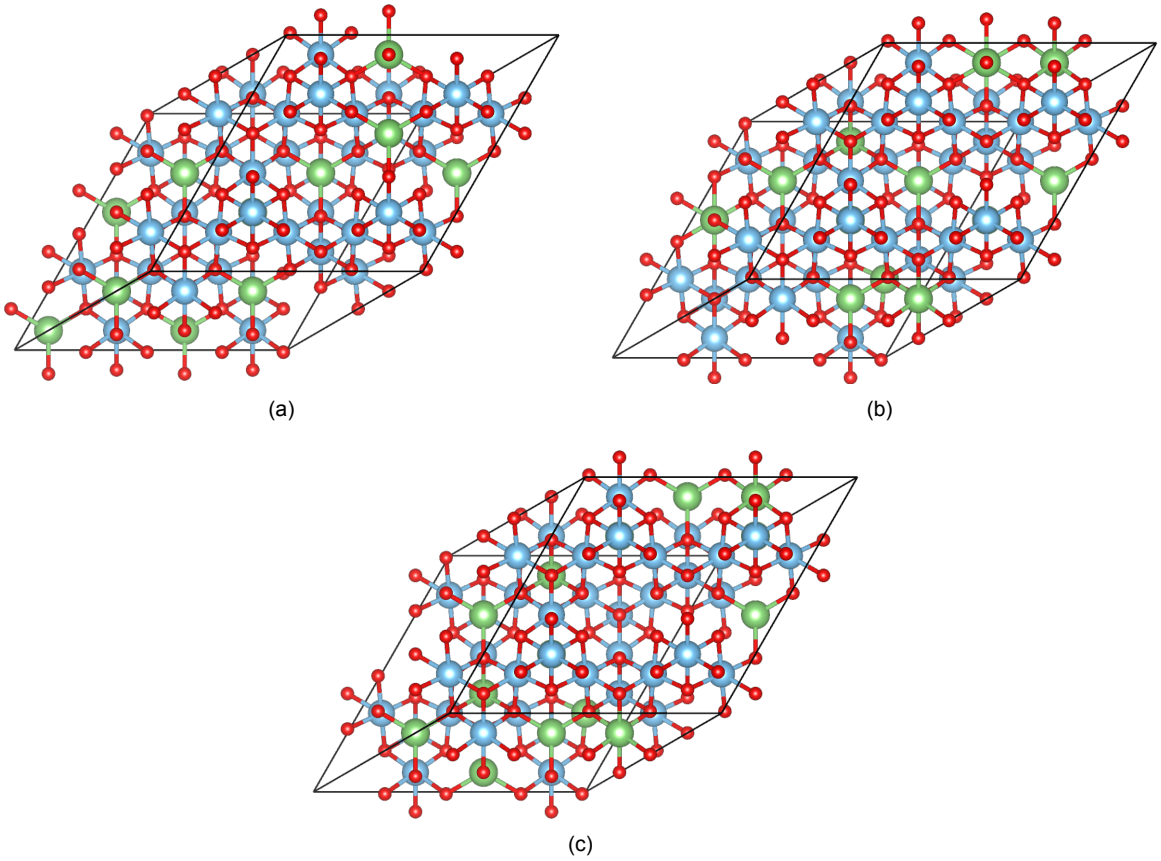


**Figure 3.4:** (a) Pristine, (b) cycled-intermediate, and (c) cycled-clustered crystal structures of $Li_{10}Ti_5O_{12}$.

By constructing a convex hull for this composition range, the thermodynamic stability of intermediate delithiated states will be determined. This is used to understand whether lithium extraction occurs through phase separation mechanisms.

To simulate acid treatment, the substitution of lithium with protons is also modeled, where the vacancies in the trial structures are now filled by $H^+$ :

$$Li_4Ti_5O_{12} \rightarrow Li_{4-x}H_xTi_5O_{12}, \quad 0 \leq x \leq 4 \tag{3.5}$$

This transformation is now visualized in Figure 3.5.

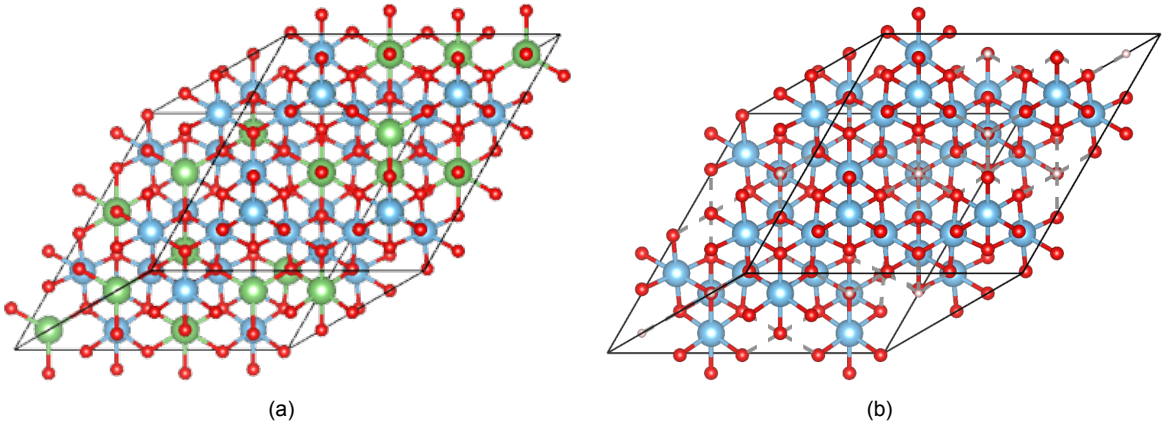


**Figure 3.5:** Unrelaxed crystal structures of (a) spinel LTO and (b) fully delithiated spinel LTO with hydrogen substitution.

Formation energies for each intermediate composition will be used to construct a third convex hull. This will help determine whether mixed Li/H phases could exist stably. The voltage profile is now determined by Equation 3.6, which incorporates the reference energy of hydrogen gas, $E_{\mathrm{H}}$.

$$\bar{V} = \frac{-\left[E_{\mathrm{H}_{2-x}\mathrm{Li}_x\mathrm{Host}} - (x-y)E_{\mathrm{Li}} - (y-x)E_{\mathrm{H}} - E_{\mathrm{H}_{2-y}\mathrm{Li}_y\mathrm{Host}}\right]}{(x-y)e} \tag{3.6}$$

## 3.3. Nudged Elastic Band Method

The Nudged Elastic Band (NEB) method is a computational technique used to find the minimum energy path (MEP) between two known states in DFT [78, 79]. NEB works by creating a series of intermediate configurations (images) of the system between the initial and final states. These images are connected by virtual springs to maintain a smooth path. The forces acting on the images are separated into two components: one along the path (due to the springs) and one perpendicular to the path (from the potential energy surface). This ensures that images are ”nudged” toward the true MEP, without sliding down to the lower energy endpoints.

To perform NEB calculations in VASP, specific INCAR settings must be added or changed to control how the images are initialized and constrained. Table 3.4 summarizes the NEB-specific INCAR tags used in this study, followed by explanations of their physical meaning and computational role:

**Table 3.4:** NEB-specific INCAR tags.

| Tag | Value |
|---|---|
| ICHAIN | 0 |
| IMAGES | 5 |
| SPRING | -5.0 |
| LCLIMB | FALSE |
| IBRION | 3 |
| POTIM | 0 |
| ISIF | 2 |
| MAXMOVE | 0.2 |
| TIMESTEP | 0.1 |

- **ICHAIN = 0.** This tag activates the nudged elastic band (NEB) method when set to 0. It instructs VASP to treat the current run as a transition path optimization problem.
- **IMAGES = 5.** This tag specifies the number of intermediate images between the initial and final configurations. These images interpolate the reaction pathway and are optimized to trace the MEP. A higher number of images can improve resolution of the path but this also increases computational cost. With `IMAGES = 5`, a total of 7 images are used (initial + 5 intermediates + final).
- **SPRING = -5.0.** This tag defines the spring constant used to connect neighboring images in the NEB path. A negative value activates improved tangent estimation, which uses an adaptive spring force to help the images distribute more evenly along the path and prevent artificial distortions. `SPRING = -5.0` is a commonly used value.
- **LCLIMB = .FALSE.** This tag controls whether the climbing image NEB (CI-NEB) is activated. When set to `.TRUE.`, the highest energy image is pushed uphill along the MEP and relaxed perpendicular to it to precisely locate the saddle point. Here, `LCLIMB = .FALSE.` means standard NEB is used without explicitly identifying the transition state.
- **IBRION = 3.** This tag sets the optimizer used to relax the NEB images. `IBRION = 3` selects the damped molecular dynamics algorithm, which gradually reduces the kinetic energy of moving atoms until the force criteria are satisfied. This method helps stabilize the motion of images along the MEP.

- **POTIM = 0.** In NEB calculations, atomic positions are updated based on the NEB force components rather than on standard ionic dynamics. Therefore, `POTIM`, which sets the ionic time step, should be set to zero to prevent unintended displacements unrelated to the NEB scheme.
- **ISIF = 2.** This tag determines what degrees of freedom are relaxed during ionic steps. `ISIF = 2` allows only the atomic positions to change, keeping the unit cell fixed. This is necessary in NEB calculations, where the goal is to trace the reaction path without allowing global deformations.
- **MAXMOVE = 0.2.** This tag sets a cap on the maximum displacement allowed per atom in each NEB step, measured in Ångströms. It helps to prevent large jumps or unstable configurations by limiting how far atoms can move in a single iteration. `MAXMOVE = 0.2` is a conservative choice for stable convergence.
- **TIMESTEP = 0.1.** In the context of `IBRION = 3`, this parameter can act as a damping factor or effective time step in the damped dynamics scheme. A smaller value like `0.1` ensures better stability and gradual convergence but may require more steps to reach the minimum.

To evaluate ion migration behavior in spinel LTO, the NEB method is applied to a series of candidate diffusion paths involving lithium and hydrogen ions. NEB calculations provide detailed insight into the energetics of these migration mechanisms by estimating the MEP and corresponding energy barriers between two known atomic configurations. The resulting energy profiles reveal the kinetic feasibility of each path and help identify the most favorable pathways.

In the context of lithium-ion diffusion, tetrahedral (8a) and octahedral (16d, 16c) sites are investigated. Figure 3.6 depicts the lithium migration paths between these sites: both direct hops between adjacent sites and multi-step mechanisms involving intermediate positions.

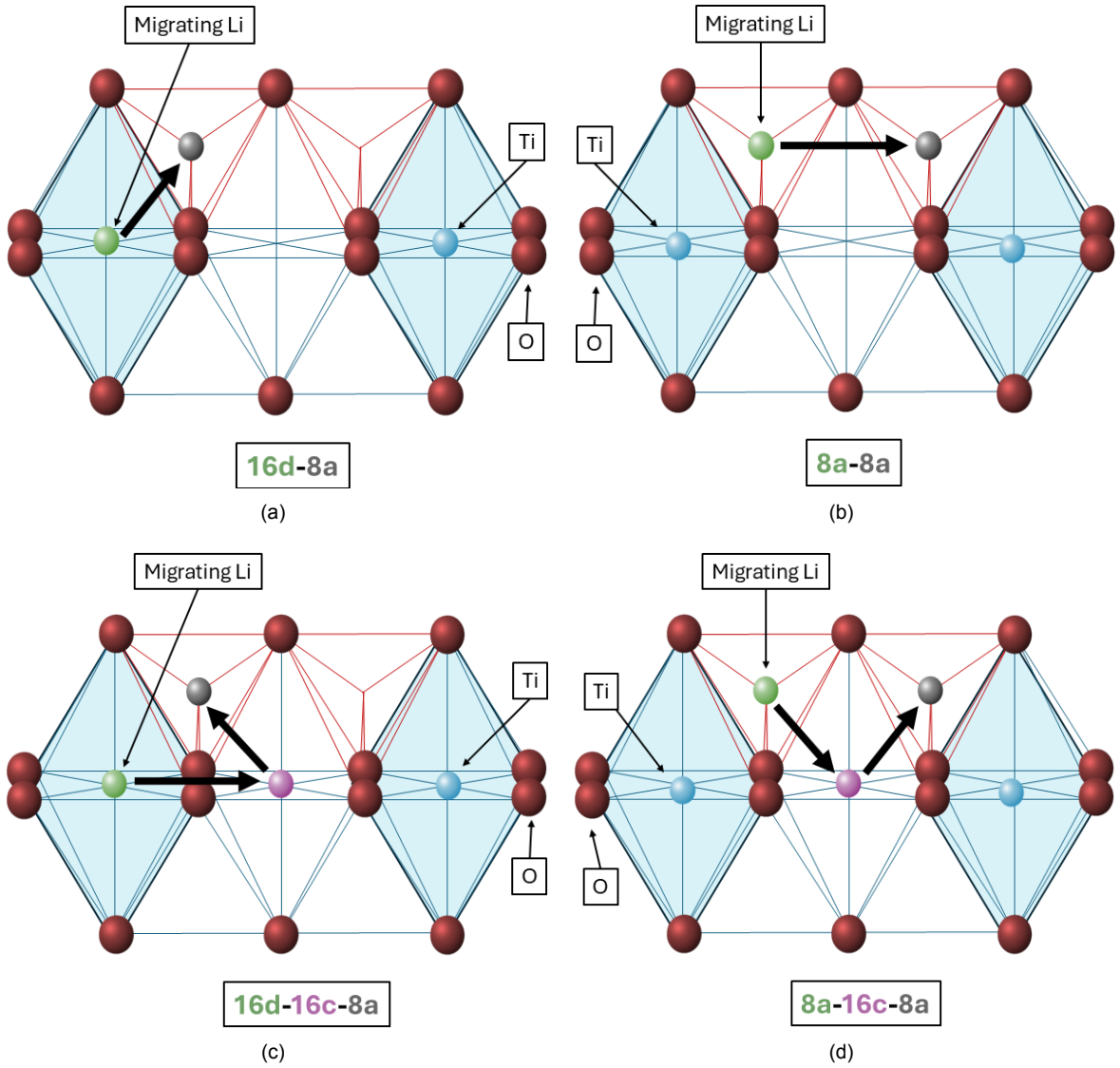


**Figure 3.6:** Possible Li migration pathways in the spinel lattice: (a) octahedral-to-tetrahedral pathway, (b) tetrahedral-to-tetrahedral pathway, (c) two-step migration pathway from 16d with an intermediate octahedral site, and (d) two-step migration pathway from 8a with an intermediate octahedral site. Green, pink, and gray spheres represent lithium ions in initial, transition, and final positions, respectively.

A separate set of NEB calculations was performed to explore hydrogen transport pathways. Figure 3.7 previews several hydrogen migration scenarios, which depend on the local lithium environment.

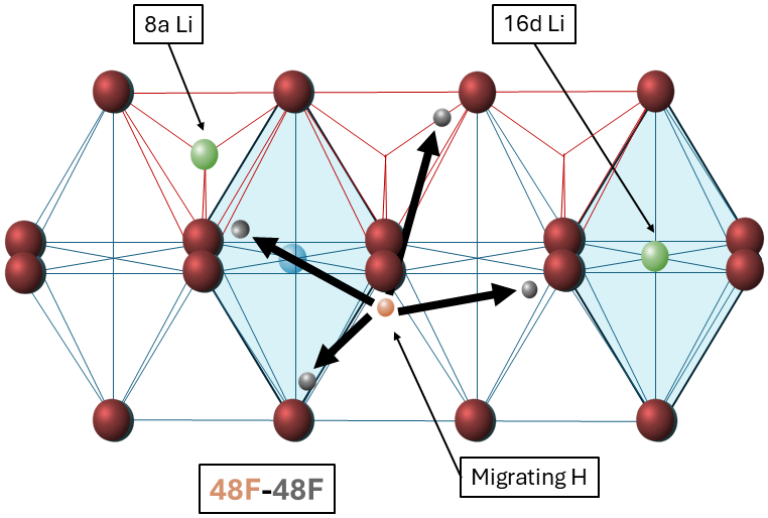


**Figure 3.7:** Possible H migration pathways in the spinel lattice. The presence (or absence) of nearby lithium in either 8a or 16d sites alters the local environment, providing different migration scenarios. Orange and gray spheres represent hydrogen ions in initial and final positions, respectively.

# 4

# Results and Discussion

This chapter presents the structural (4.1), thermodynamic (4.2), and kinetic (4.3) response of spinel LTO during lithium removal and hydrogen-assisted exchange. Three composition series are analyzed: (i) vacancy-driven delithiation ($\mathrm{Li}_n\mathrm{Ti}_{24}\mathrm{O}_{64}$), (ii) hydrogen-substituted delithiation ($\mathrm{H}_{21-n}\mathrm{Li}_n\mathrm{Ti}_{24}\mathrm{O}_{64}$), and (iii) lithium insertion beyond the stoichiometric end member. Structural evolution is quantified by tracking local bond metrics, cell volumes, and lattice parameters. Thermodynamic behavior upon delithiation is evaluated via total energies, convex-hull analyses, and derived voltage profiles. Ion-migration pathways for $Li^+$ and $H^+$ are identified using NEB calculations to determine kinetically preferred routes and potential rate-limiting steps.

Analyses center on the two delithiation series; the insertion series is included primarily as a reference, given the extensive existing literature on LTO insertion. To represent possible cycling histories, each composition can be evaluated in three arrangements: pristine (maximally dispersed Li), cycled–intermediate, and cycled–clustered (maximal Li aggregation). Data are taken from fully relaxed supercells, and results are deemed converged when the numerical ionic error is $\mathcal{O}(10^{-4})$.

Overall, the structural analysis shows that while local Li–O and Ti–O coordination environments remain robust to delithiation, hydrogen substitution, and cycling history, the unit-cell volume accommodates the structural response. Proton incorporation mitigates expansion and helps maintain near–zero-strain behavior, while Li clustering amplifies volume changes. Thus, homogeneous lithium distribution and controlled protonation emerge as practical design levers to preserve structural stability and durability of spinel LTO in lithium-sieving applications.

Thermodynamic analysis reveals that hydrogen consistently stabilizes delithiated frameworks, lowering the slope of total energy versus delithiation step relative to vacancy counterparts. Both vacancy and H-substituted series favor a solid-solution pathway, avoiding long-lived two-phase regions that would otherwise slow $Li^+$ transport. This is especially true for the H-substituted series, where metastable points are consistently closer to the hull than in the vacancy series. Li clustering is disfavored, with clustered variants lying farther above the convex lines. Therefore, homogeneous delithiation and proton incorporation promote smoother, more stable thermodynamics that support efficient and durable lithium-sieving operation.

Ion-migration analysis identifies the 16c site as a kinetic bridge that enables $Li^+$ to traverse the tetrahedral network with activation barriers below 0.5 eV, while direct 8a–8a and 8a–16d hops are prohibitively slow and become especially prohibitive when the sites are nonadjacent. Octahedral 16d Li remains largely immobile. $H^+$ motion along 48f–48f pathways also presents a challenge, with barriers $\geq$1.9 eV and a strong dependence on path length, suggesting that proton transport may be the rate-limiting step of the exchange cycle.

## 4.1. Structural Evolution

To account for possible structural rearrangements during use of the sieve, three classes of configurations are analyzed: pristine, cycled-intermediate, and cycled-clustered. Pristine structures have maximally dispersed Li atoms, corresponding to minimized electrostatic repulsion. Cycled-clustered configurations exhibit maximal Li clustering, serving as a limiting case to assess the effects of severe inhomogeneity that could develop under extended cycling. Cycled-intermediate structures reflect a moderate degree of lithium aggregation, representing a transitional state between the pristine and clustered extremes.

Following relaxation, the tetrahedral Li–O bond lengths remain largely unchanged throughout all delithiation steps, stabilizing near 1.98 to 1.99 Å. These distances are nearly identical to those of the unrelaxed super-cells. This can be seen by comparing Figure 3.3 to the relaxed structures in Figures 4.1a and 4.1b. Octahedral Li–O distances expand from 1.99 to 2.10-2.30 Å. Ti–O bond lengths also deviate slightly from the initial 1.99, spanning 1.90 to 2.20 Å after relaxation.

In the hydrogen-substituted series, protons initially occupying the 8a site (Figure 3.5b) migrate to the 48f site upon relaxation, forming O–H bonds of 0.98 Å (Figure 4.1c). This relocation is consistent across all compositions studied.

No systematic differences are observed between cycled and pristine variants; both exhibit the same range of Li–O and Ti–O bond lengths and display identical proton relocation behavior as shown in Figure 4.2.

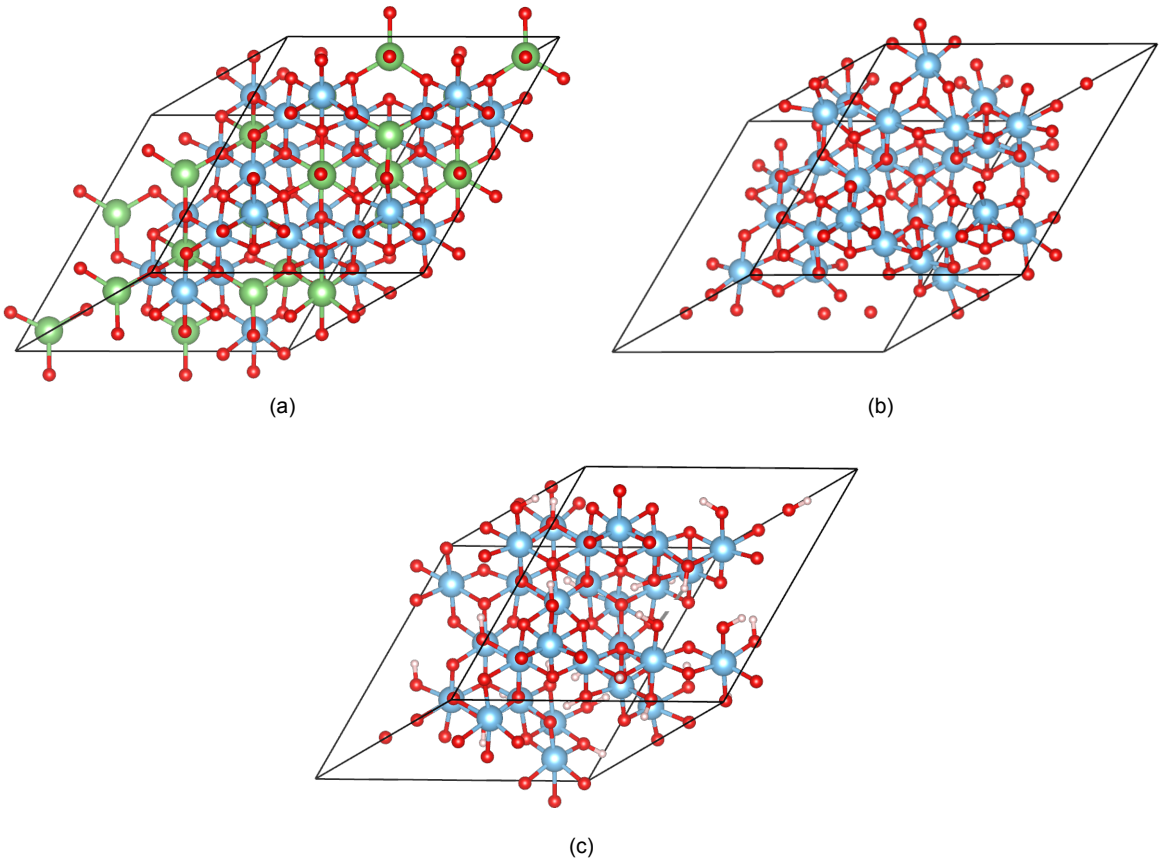


**Figure 4.1:** Relaxed end configurations of the delithiation transformations: (a) $Li_{21}Ti_5O_{12}$, (b) $Li_0Ti_5O_{12}$, and (c) $H_{21}Li_0Ti_5O_{12}$.

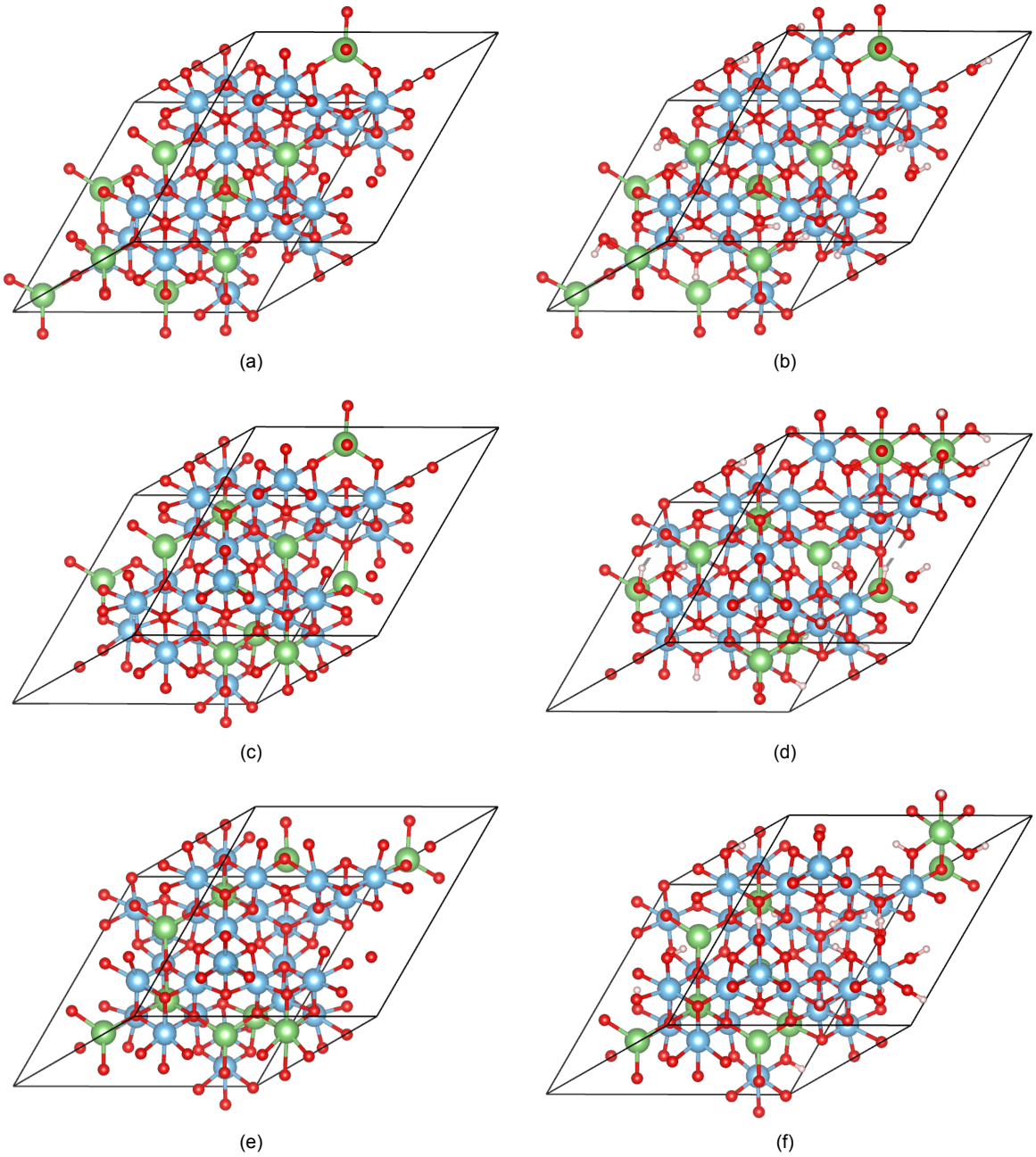


**Figure 4.2:** Relaxed pristine and cycled crystal structures of $Li_{10}Ti_5O_{12}$ with vacancies and with hydrogen substitution: (a) Pristine, (b) Pristine + H, (c) Cycled-intermediate, (d) Cycled-intermediate + H (e) Cycled-clustered, and (f) Cycled-clustered + H.

The 1168.37 Å$^3$ supercells of all configurations all increased in volume after relaxation, with $Li_{37}Ti_{24}O_{64}$ increasing the least to 1174.86 Å$^3$. Figure 4.3 compares the cell-volume change that accompanies lithium removal for the relaxed vacancy (blues) and H-substituted (reds) series and the lithium insertion process (green). Only the thermodynamically stable configurations (explained in section 4.2) are plotted.

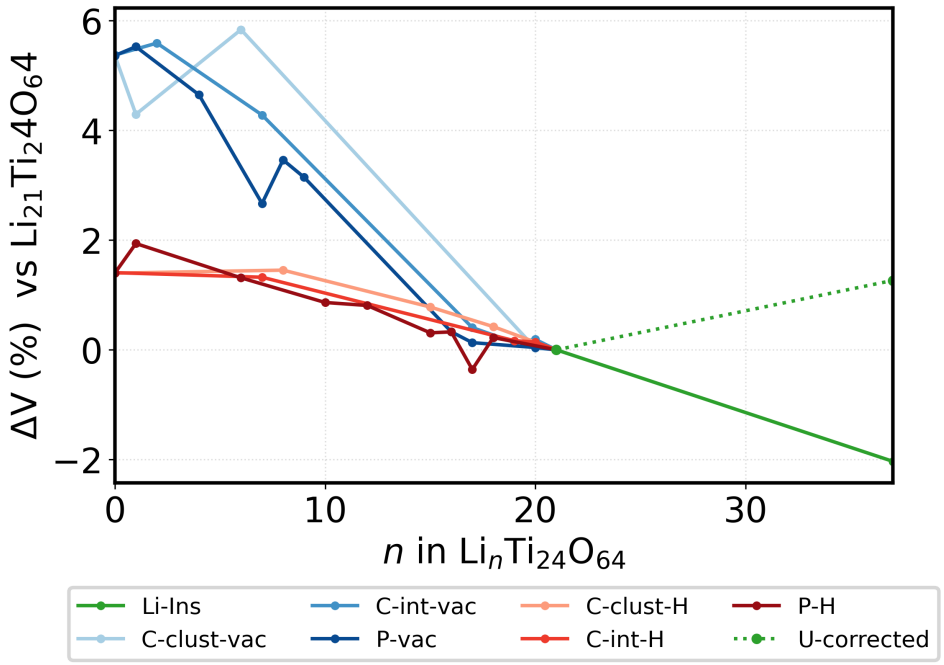


**Figure 4.3:** Volume change of pristine and cycled configurations with respect to $Li_{21}Ti_{24}O_{64}$ for $H_{21-n}Li_nTi_{24}O_{64}$ ($0 \leq n \leq 21$) and $Li_nTi_{24}O_{64}$ ($0 \leq n \leq 37$).

In modeling the delithiation and Li-insertion process, all series start from the same fully-lithiated volume of 1199.24 Å$^3$ at $n = 21$. As the pristine vacancy series (denoted by P-vac) is delithiated, the volume rises and reaches 1263.58 Å$^3$ at $n = 0$, an expansion of about 5.4%. The pristine H-substituted series (P-H) expands less, ending at 1216.01 Å$^3$, or roughly 1.4%. A zero-strain material is usually taken to show no more than a 1% change, so proton substitution keeps the lattice closer to this benchmark.

The cycled variants, labeled C-clust (high Li clustering) and C-int (intermediate clustering), generally exhibit larger volume changes than their darker colored pristine counterparts do. This discrepancy is smaller for the hydrogen substitution series (reds), and at all of the lithiation extremes, where the structures are most alike, and grows with the degree of Li clustering. Since cycled variants show larger volume swings, synthesis and operating strategies should aim to promote homogeneous lithiation.

For the Li-insertion series, two trends are shown: one calculated without a Hubbard $U$ correction, and one with it applied to Ti 3$d$ states ($U = 4.5$ eV [80, 81]). Without $U$, the structure contracts, in disagreement with experimental observations for spinel LTO. This unphysical contraction arises because, in standard GGA, the electrons introduced upon lithiation are overly delocalized across the Ti sublattice, producing averaged oxidation states rather than discrete $Ti^{3+}$ and $Ti^{4+}$ sites. Introducing a Hubbard $U$ mitigates this self-interaction error by localizing the inserted electrons on Ti, restoring discrete $Ti^{3+}$ centers and yielding the experimentally consistent lattice expansion (in this case 1252.12 to 1267.96 Å$^3$) upon lithium insertion.

By contrast, the delithiation series is reported without $U$ for two reasons. First, applying $U$ worsens voltage accuracy: the calculated average voltage shifts from 1.43 V (GGA) to 1.84 V (GGA+$U$), whereas experiments report $\sim$ 1.55 V [76]. Second, $U$ has limited leverage over the hydrogen substituted delithiation pathway; only a single $Ti^{3+}$ center is present, making a Ti 3$d$ Hubbard term less consequential. Accordingly, GGA+$U$ is used only to check for correct insertion contraction, while GGA is kept for delithiation to preserve voltage accuracy. In Figure 4.3, each curve is referenced to its own $n = 21$ baseline computed with the same functional (GGA or GGA+$U$).

For the on-hull compositions (explained in subsection 4.2.1), the lattice parameters are also plotted (Figure 4.4) to check for anisotropic effects. During delithiation, the lattice parameters of spinel $Li_4Ti_5O_{12}$ evolve in a relatively uniform manner. The largest ratio between lattice parameters is about 1.025, indicating that the relative changes across different directions remain very small. In contrast, anisotropic

layered oxides have lattice parameter ratios spanning 4.85 to 5.15, reflecting directional dependence in their structural response [82]. This comparison highlights that the delithiation of spinel LTO can be regarded as effectively isotropic.

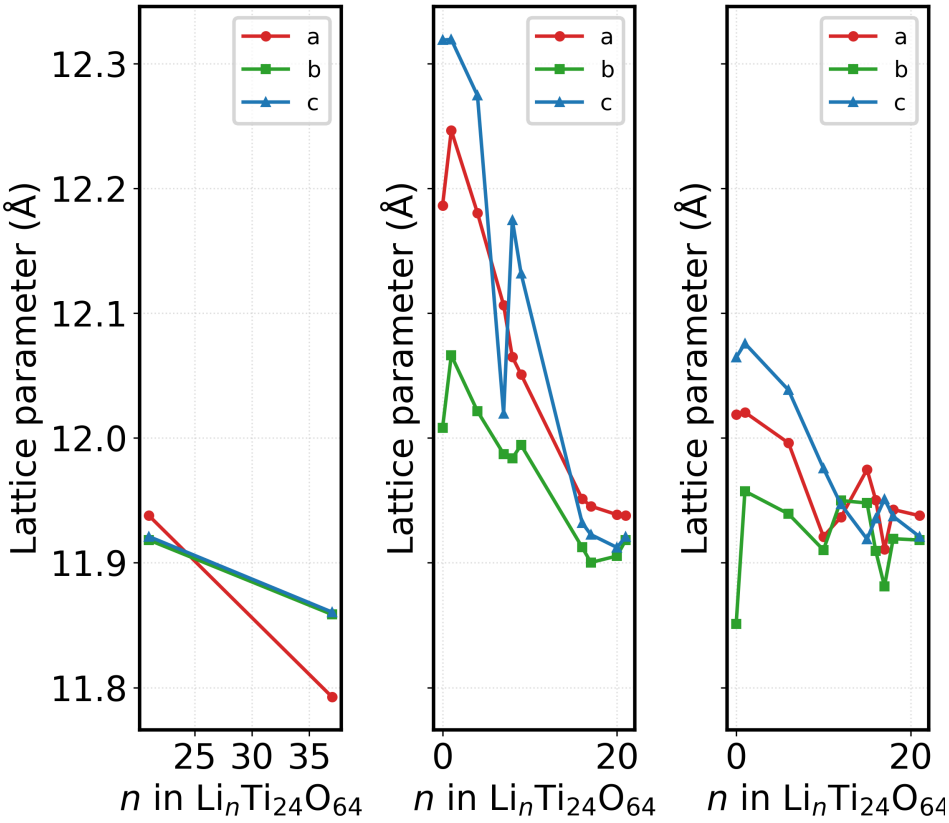


**Figure 4.4:** Lattice parameters $H_{21-n}Li_nTi_{24}O_{64}$ $(0 \leq n \leq 21)$ and $Li_nTi_{24}O_{64}$ $(0 \leq n \leq 37)$.

Across all structures examined (pristine, cycled-intermediate, and cycled-clustered) the local coordination shells remain essentially invariant. The Li–O and Ti–O bond-length ranges are the same regardless of configuration or cycling history, and H always relaxes from the 8a vicinity to form O–H at the 48f site. In other words, the local polyhedra geometry is robust to both delithiation state and cycling, while the cell volume is the degree of freedom that carries the structural response. This suggests that in spinel LTO the cell volume is set by the packing of the (nearly rigid) $TiO_6$ octahedra and $LiO_4$ tetrahedra. Changes in polyhedral tilt and linkage angles can change the lattice constant even when the internal bond-length ranges remain the same.

The larger volume increases in cycled states argue for synthesis and protocols that suppress Li aggregation, such as smaller particles and moderate rates with longer equilibration to smooth concentration gradients. In summary, the local framework of spinel LTO is structurally resilient across states of charge and cycling; the actionable descriptor is the volume evolution. Operationally, promoting homogeneous Li distributions and protonation offers a practical route to maintain near–zero-strain behavior and, by extension, durability in lithium-sieving applications.

## 4.2. Thermodynamics Upon Delithiation

Figure 4.5 compares the unnormalized total energies of the vacancy (blues), H-substituted (reds), and Li-insertion (green) structures across the full delithiation and insertion range.

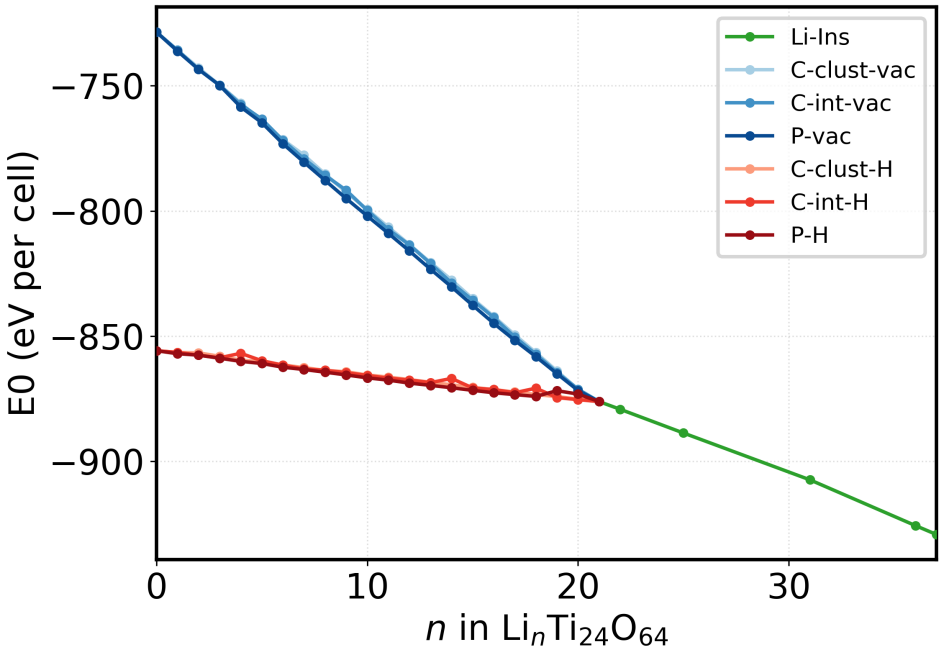


**Figure 4.5:** Total energies for $H_{21-n}Li_nTi_{24}O_{64}$ $(0 \leq n \leq 21)$ and $Li_nTi_{24}O_{64}$ $(0 \leq n \leq 37)$ .

In both the vacancy and hydrogen-substituted delithiation series, the total energy increases as lithium is removed. The steeper slope observed in the vacancy series (blue curves) suggests a larger energy increase per removed Li atom compared to the hydrogen-substituted case (red curves). This implies that structures with vacancies experience a stronger energetic penalty from further delithiation, at least within the raw DFT energy landscape.

Across both series, cycled variants (blue, red, light blue, and light red) generally lie slightly above their pristine counterparts (dark blue and dark red). Although small in relative magnitude, such differences signal marginal destabilization with repeated use.

### 4.2.1. Convex Hulls

While total energies reflect the relative stability of individual configurations, convex hulls provide deeper insight into the thermodynamic stability and phase behavior of a series. Figure 4.6 displays the convex hulls that describe the stability of all calculated compositions.

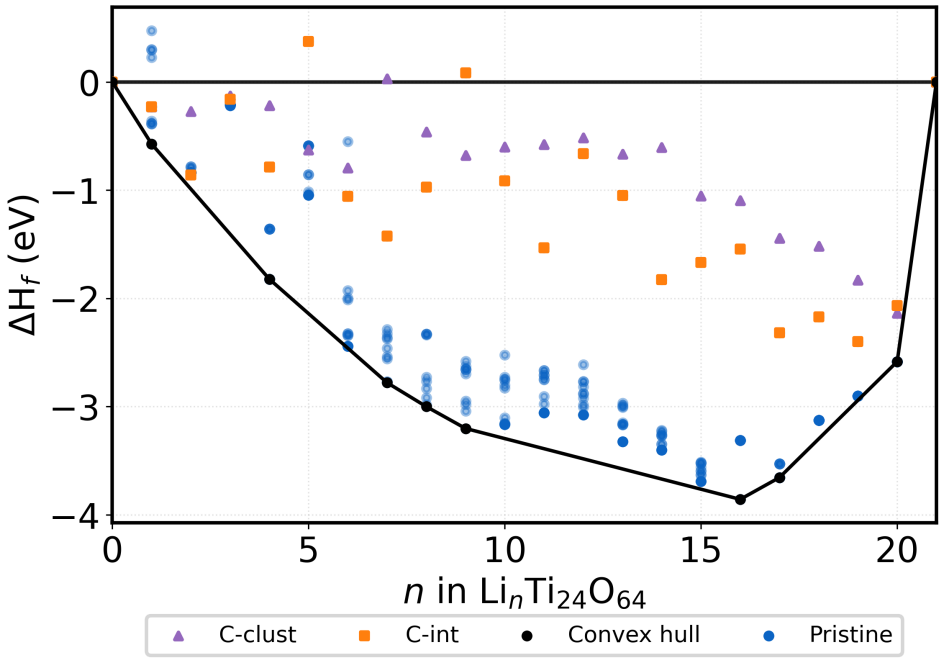


(a)

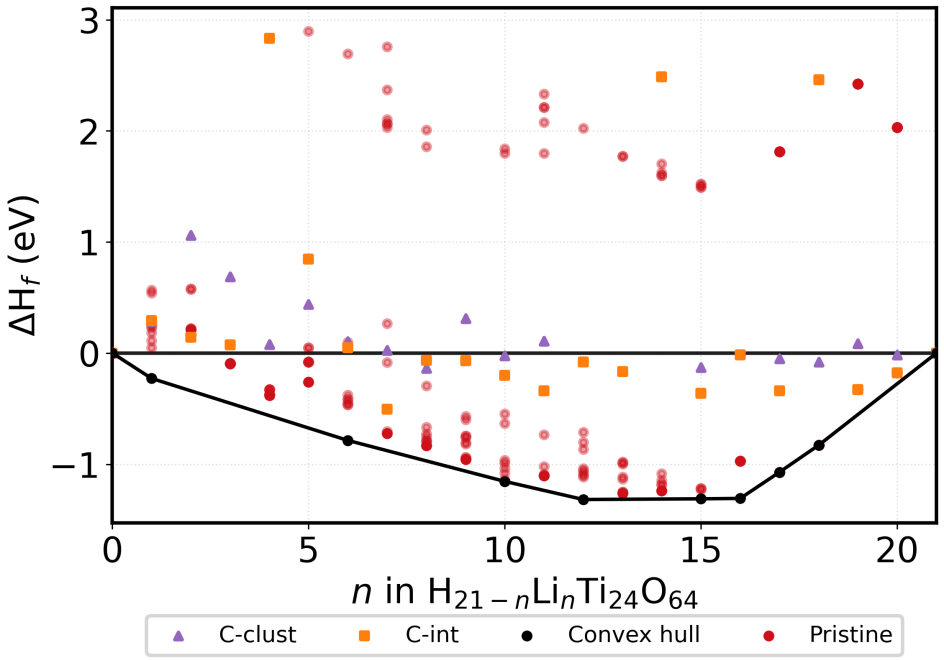


(b)

**Figure 4.6:** Convex hulls for (a) $Li_nTi_{24}O_{64}$ and (b) $H_{21-n}Li_nTi_{24}O_{64}$ ($0 \leq n \leq 21$).

Both convex-lines (black) lack a pronounced global minimum and instead comprise several shallow vertices. While a few narrow two-phase tielines do appear, the compositions bridging them often sit within 25 meV/atom of the hulls, especially in the hydrogen-substituted hull. At typical operating temperatures, such small energetic offsets could be surmounted, so a solid-solution response is still expected. This is advantageous: with no long-lived two-phase miscibility gap, lithium can diffuse through the lattice unimpeded by a slow, migrating interface [83]. Generally, avoiding such two-phase transitions also reduces mechanical stress and damage to the lattice, which improves cycle life. A modest tem-

perature rise may smooth any residual two-phase behavior. The cycled variants (C-clust and C-int) are appreciably less accessible for both series; their energies sit farther above the hulls, which are in both series found to be formed by pristine compositions only, and the penalty grows with the degree of Li-clustering. This indicates that Li aggregation is thermodynamically disfavored. An exception arises in the hydrogen-substituted series: during the first two delithiation steps ($\mathrm{H_1Li_{20}Ti_{24}O_{64}}$ and $\mathrm{H_2Li_{19}Ti_{24}O_{64}}$), the cycled variants are more accessible than the pristine ones. This suggests that, at low hydrogen concentrations, stability is governed less by maximizing Li–Li spacing. Note also that fewer pristine variants are present in these early steps because the structure-generation script saved trial structures with duplicates. The most favorable Li-spaced configurations in this regime remove $16d$ sites in a specific order, which led to single variants being saved multiple times.

### 4.2.2. Voltage Profiles

The reference energies for bulk lithium and hydrogen gas were obtained from separate DFT relaxations:

$$E_{\mathrm{Li}} = -1.89 \text{ eV atom}^{-1} \quad \text{(per Li atom in bulk Li)}$$
$$E_{\mathrm{H}} = -3.39 \text{ eV atom}^{-1} \quad \text{(per H atom in } \mathrm{H_2} \text{ gas)}$$

Hydrogen gas is used as the reference state because it represents the most stable elemental phase of hydrogen. These values are used in Equations 3.2 and 3.6 to plot the voltage profiles seen in Figure 4.7.

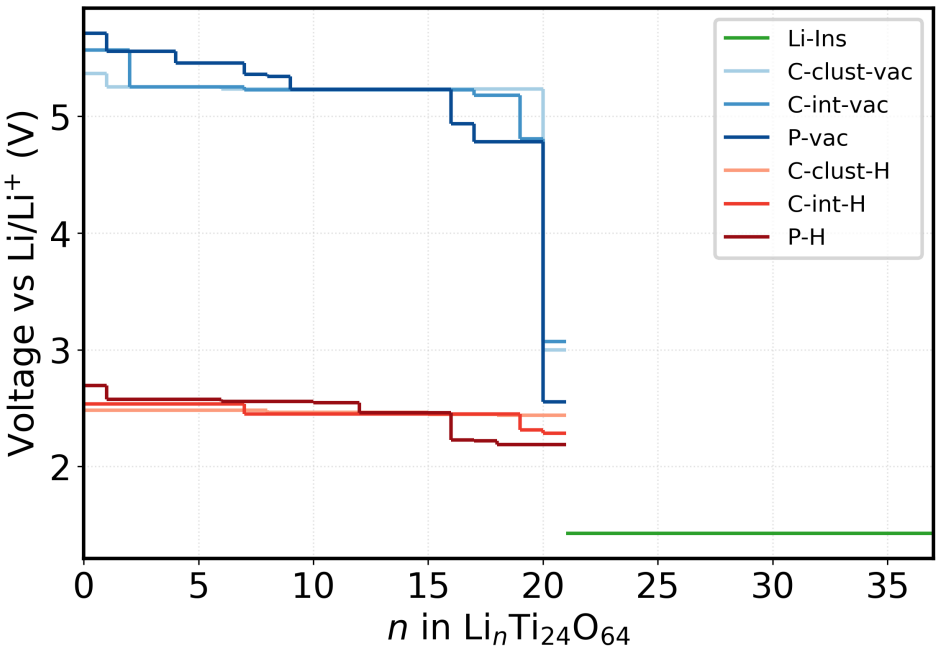


**Figure 4.7:** Average extraction voltage $\bar{V}$ versus composition for $\mathrm{H_{21-n}Li_nTi_{24}O_{64}}$ $(0 \leq n \leq 21)$ and $\mathrm{Li_nTi_{24}O_{64}}$ $(0 \leq n \leq 37)$.

All calculated voltages are positive, indicating that Li insertion is thermodynamically favorable relative to the Li bulk reference. Overall, the vacancy series exhibits larger voltage magnitudes than the hydrogen-substitution series, reflecting a stronger thermodynamic driving force for Li retention.

In the hydrogen-substitution series, the voltage increases gradually between successive tielines with delithiation, rising from 2.187 V for the initial step $\mathrm{Li_{21}Ti_{24}O_{64}} \rightarrow \mathrm{H_3Li_{18}Ti_{24}O_{64}}$ to 2.692 V for the final step $\mathrm{H_{20}Li_1Ti_{24}O_{64}} \rightarrow \mathrm{H_{21}Ti_{24}O_{64}}$. By contrast, the vacancy series shows a much sharper initial increase, jumping from 2.553 V for $\mathrm{Li_{21}Ti_{24}O_{64}} \rightarrow \mathrm{H_1Li_{20}Ti_{24}O_{64}}$ to 4.780 V for $\mathrm{Li_{20}Ti_{24}O_{64}} \rightarrow \mathrm{Li_{17}Ti_{24}O_{64}}$, followed by a more gradual rise to 5.709 V for the final step $\mathrm{Li_1Ti_{24}O_{64}} \rightarrow \mathrm{Ti_{24}O_{64}}$.

When cycling is considered, both pathways retain similar voltage magnitudes and growth patterns to the pristine systems, but the cycled variants exhibit fewer voltage steps. These extended voltage plateaus

are generally unfavorable because they correspond to broad two-phase regions rather than to solid solution. In electrochemical sieving applications, a smoother, more stepwise profile is easier to control, provides a clearer indication of lithium content, and reduces the risk of hysteresis inefficiencies.

## 4.3. Ion Migration

To map how $Li^+$ and $H^+$ move during hydrogen-assisted delithiation, nudged elastic band (NEB) calculations were performed on five representative pristine $\mathrm{Li}_x\mathrm{H}_y\mathrm{Ti}_{27}\mathrm{O}_{64}$ compositions: $\mathrm{Li}_{21}\mathrm{H}_0\mathrm{Ti}_{27}\mathrm{O}_{64}$ ($Li^+$ migration in a Li-rich host), $\mathrm{Li}_0\mathrm{H}_{21}\mathrm{Ti}_{27}\mathrm{O}_{64}$ ($H^+$ migration in an H-rich host), and the mixed states $\mathrm{Li}_6\mathrm{H}_{15}\mathrm{Ti}_{27}\mathrm{O}_{64}$, $\mathrm{Li}_{12}\mathrm{H}_9\mathrm{Ti}_{27}\mathrm{O}_{64}$, and $\mathrm{Li}_{16}\mathrm{H}_5\mathrm{Ti}_{27}\mathrm{O}_{64}$. On the hydrogen-substituted convex line (Figure 4.6b), these compositions include the Li-rich and H-rich end members, the plateau tie-line end points, and an intermediate state ($\mathrm{Li}_6\mathrm{H}_{15}\mathrm{Ti}_{27}\mathrm{O}_{64}$) that lies within the broadest potentially two-phase region.

Unlike convex hull and voltage profile calculations, vacancy NEB calculations would not provide a meaningful upper bound on lithium migration barriers. Removing lithium without charge compensation reduces Coulombic repulsion and has been shown to expand the lattice (Figure 4.3), potentially lowering migration barriers rather than raising them. For this reason, kinetic studies were restricted to the hydrogen-substitution pathway, which reflects the ion-exchange mechanism.

Alternative crystallographic pathways are compared to identify which sites are kinetically prioritized by the reaction. For $Li^+$, direct 8a $\rightarrow$ 8a or 8a $\rightarrow$ 16d hops and two-step mechanisms involving 16c intermediates are evaluated. For $H^+$, 48f $\rightarrow$ 48f translations are evaluated. Together, these results aim to reveal which Li/H sites are favored as ion exchange proceeds and whether hydrogenation reshapes the Li migration landscape.

### 4.3.1. Lithium Migration

The discussion first examines $Li^+$ migration from a tetrahedral 8a site, contrasting the direct 8a $\rightarrow$ 8a hop with the 8a $\rightarrow$ 16d transition to identify the more kinetically accessible destination. Figure 4.8 is a POSCAR snapshot in which the atomic positions from all NEB images are overlaid to visualize two competing $Li^+$ trajectories starting from the same 8a site (dark blue). Yellow markers trace the direct 8a $\rightarrow$ 8a pathway between neighboring tetrahedra, while orange markers trace the alternative route toward a nearby 16d octahedral site. Bonds are omitted to keep the paths legible.

Figure 4.9 compares the NEB barriers for direct 8a $\rightarrow$ 8a hops (solid lines) and 8a $\rightarrow$ 16d transitions (dotted lines) across the sampled compositions. The four 8a-16d barriers display a wide spread, from 6.414 eV in $\mathrm{Li}_{21}\mathrm{Ti}_{27}\mathrm{O}_{64}$ to 37.431eV in $\mathrm{Li}_{12}\mathrm{H}_9\mathrm{Ti}_{27}\mathrm{O}_{64}$. By contrast, the 8a $\rightarrow$ 8a barriers are tightly clustered between 0.622 eV and 0.696 eV. This indicates that, even under the best-case scenario of the sampled environments, adjacent 8a sites are far more kinetically accessible by direct hopping than nearby 16d sites. In fact, these 8a $\rightarrow$ 16d barriers render the 16d site effectively inaccessible on experimental timescales.

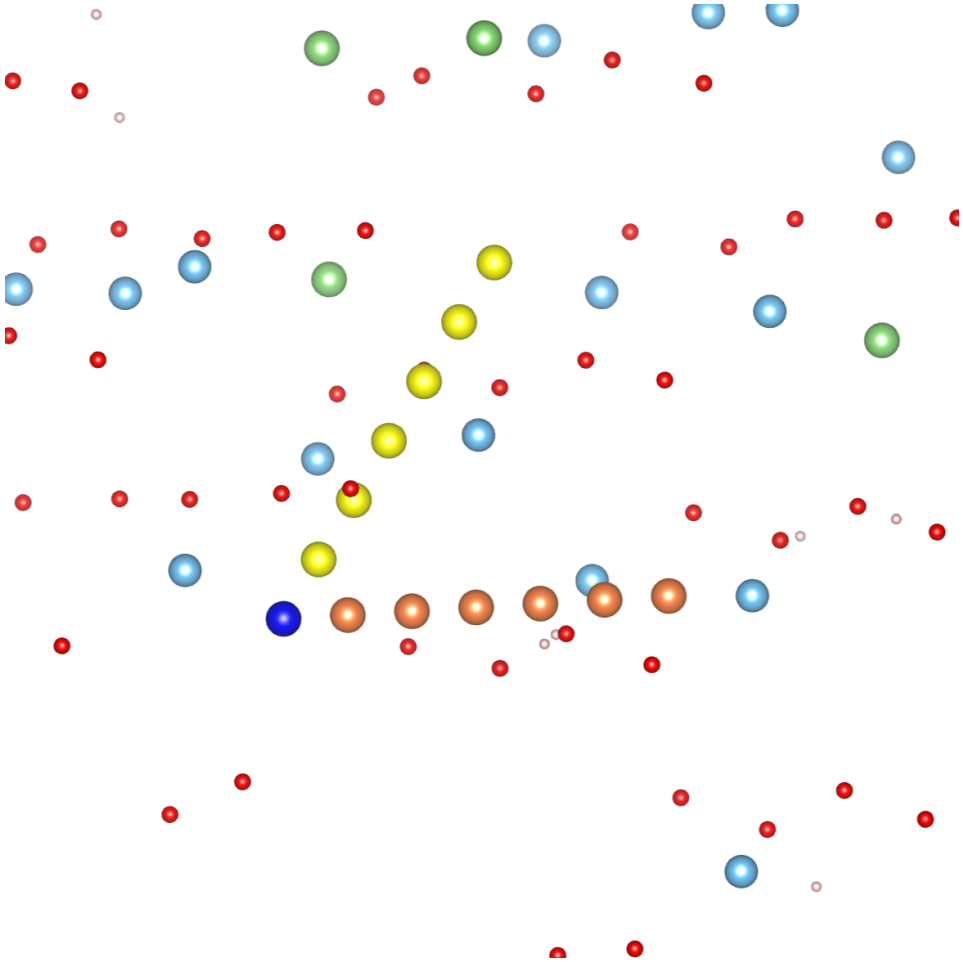

**Figure 4.8:** NEB-relaxed $Li^+$ diffusion pathways: direct 8a–8a (yellow) and 8a–16d migration (orange), both originating from the dark blue Li atom.

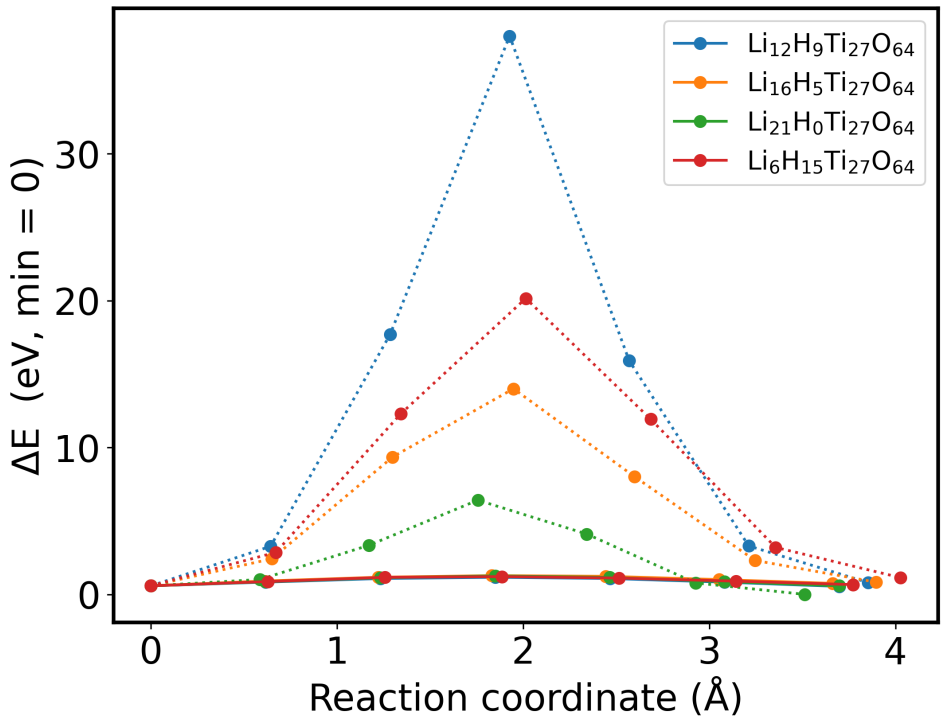


**Figure 4.9:** Energy barriers for Li diffusion from the 8a site to neighboring 8a (solid lines) and 16d (dotted lines) positions in various Li-H-Ti-O compositions

To test whether Li might also traverse between non-neighboring 8a sites in a single step, Figure 4.10 plots two 8a → 8a hops in $Li_6H_{15}Ti_{24}O_{64}$ with greater final reaction coordinates. Both exhibit barriers of the same order as the 8a → 16d case, and are therefore likewise not feasible as single-step events.

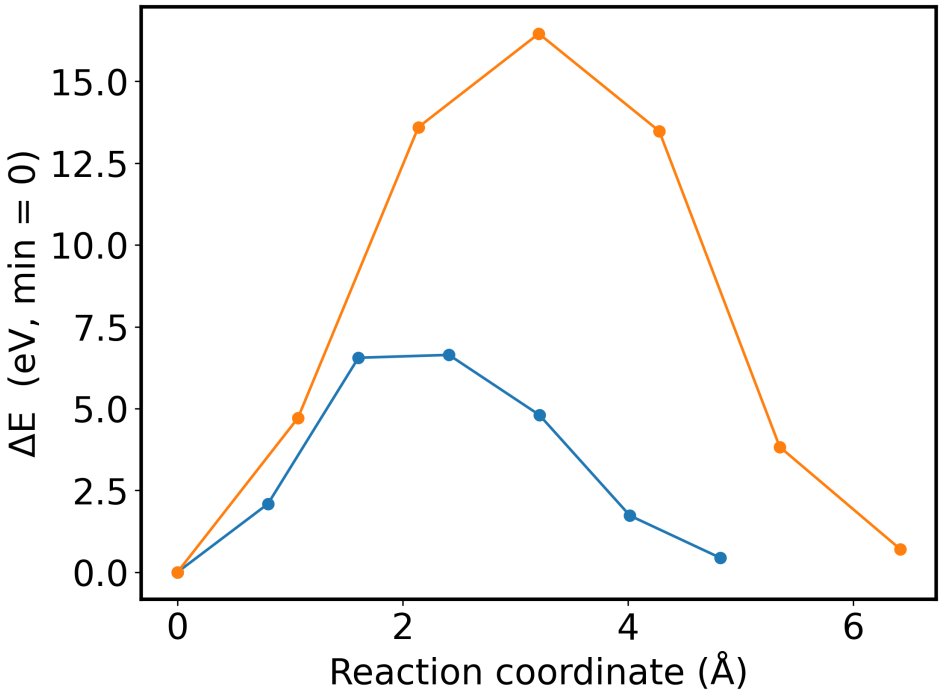


**Figure 4.10:** Energy barriers for Li migration along non-adjacent 8a → 8a diffusion paths in $Li_6H_{15}Ti_{24}O_{64}$.

These results motivate the next analysis, which considers multi-step pathways that leverage the metastable 16c site. This is done to assess whether direct 8a → 8a diffusion between adjacent tetrahedra is the true preferred mechanism and whether $Li^+$ migration can take place to and from the 16d site.

Figure 4.11 provides a POSCAR-style overlay of all NEB images to contrast the direct 8a → 8a hop (yellow) with the intermediate-step 8a → 16c pathway (orange). The starting $Li^+$ is shown in blue. The early segments of the two trajectories nearly coincide, but diverge slightly as the images progress along the paths.

Figure 4.12 displays the corresponding barriers across the sampled compositions. For the via-16c pathways in Figure 4.12, the NEB was computed for the half-step 8a → 16c and then mirrored about the 16c image to construct the composite 8a → 16c → 8a curve. This construction is allowed because the minimum-energy path on a potential-energy surface is direction-independent. In every case, routing through the 16c intermediate lowers the activation energy (now between 0.31 and 0.47 eV) relative to the direct 8a → 8a hop, indicating that the minimum-energy migration pathway between adjacent 8a sites proceeds via 16c.

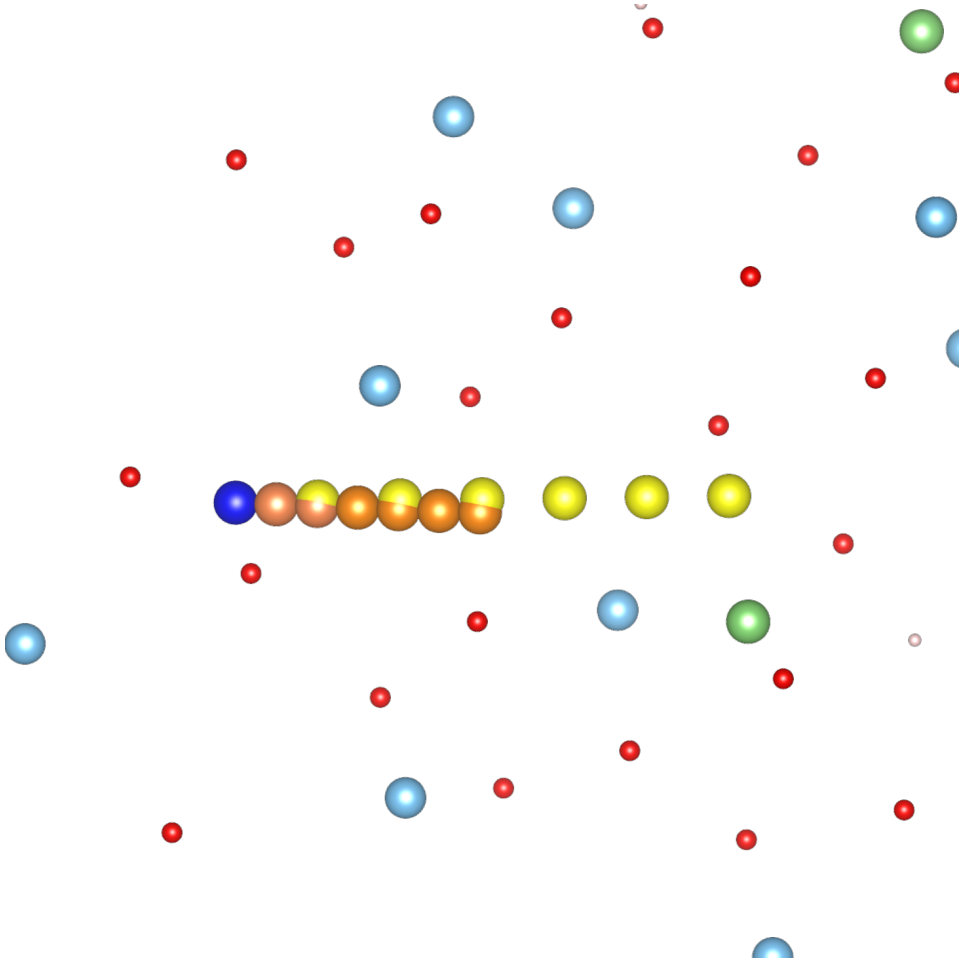

**Figure 4.11:** NEB-relaxed Li diffusion pathways: direct 8a → 8a hopping (yellow) and two-step 8a → 16c migration via intermediate 16c site (orange). The starting Li position is shown in blue.

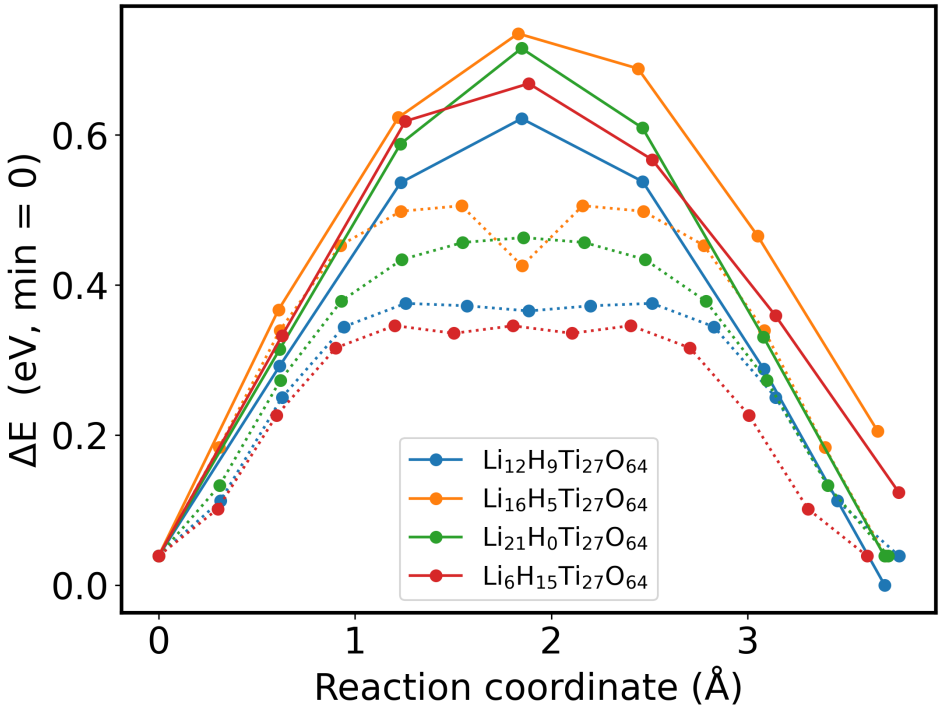


**Figure 4.12:** Energy barriers for Li diffusion between adjacent 8a sites via direct hopping (solid lines) and via an intermediate 16c site (8a → 16c → 8a, dotted lines) for various Li-H-Ti-O compositions.

Figure 4.13 shows the barriers between the 16d octahedral site and the 16c intermediate in $Li_6H_{15}Ti_{24}O_{64}$. Compared with the direct 8a $\rightarrow$ 16d route discussed above, routing through 16c yields a drastic reduction in the relevant activation barrier: the two traces peak at $\sim 1.4$ and $\sim 1.6$ eV. These results suggest that when $Li^+$ leaves a 16d environment, progression via the 16c pocket is the more kinetically viable gateway toward neighboring tetrahedral sites. However, these values still suggest the site is highly inactive at room temperature. A caveat is that only two NEB calculations produced meaningful results for this comparison, both in $Li_6H_{15}Ti_{24}O_{64}$, so additional compositions should be evaluated to improve generality.

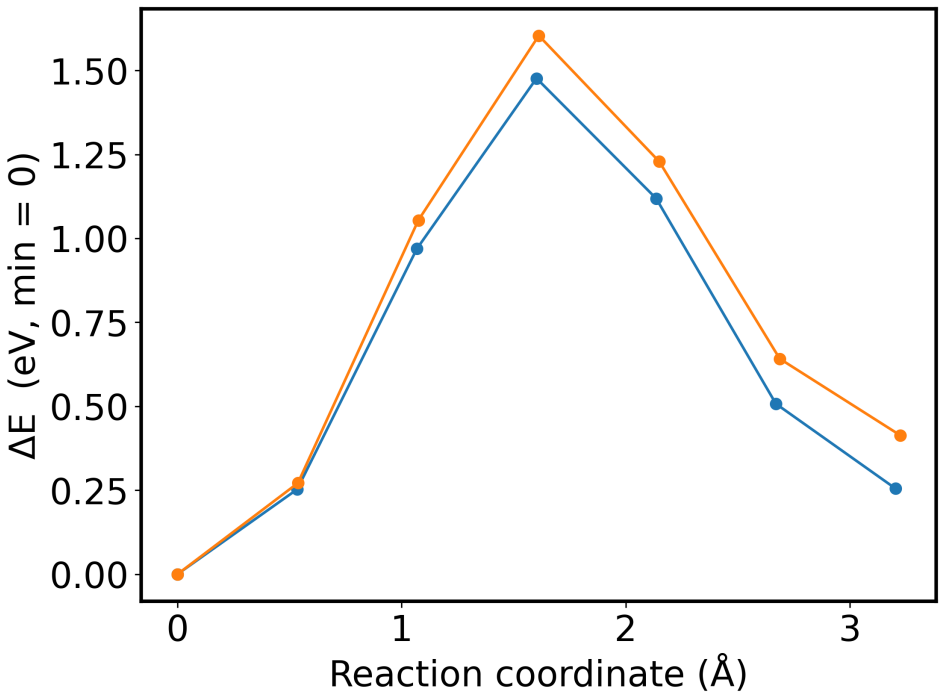


**Figure 4.13:** Energy barriers for Li diffusion between 16d and intermediate 16c sites in $Li_6H_{15}Ti_{24}O_{64}$.

### 4.3.2. Hydrogen Migration

The $H^+$ 48f $\rightarrow$ 48f dataset was generated in two compositions, $Li_0H_{21}Ti_{27}O_{64}$ and $Li_6H_{15}Ti_{27}O_{64}$. Hops were grouped by the cation polyhedron hosting the oxygen sites into three classes: (i) O on a Li-centered tetrahedron ($LiO_4$), (ii) O on a Li-centered octahedron ($LiO_6$), and (iii) O on a Ti-centered octahedron ($TiO_6$). The initial and final sites can belong to the same class or different classes, so the dataset spans both intra-class transfers (for instance $LiO_4 \rightarrow LiO_4$, $TiO_6 \rightarrow TiO_6$) and cross-class transfers ($LiO_4 \leftrightarrow LiO_6$, $LiO_4 \leftrightarrow TiO_6$, LiO6$\leftrightarrow$TiO6). These classes include both occupied and vacant Li-centered sites, as both scenarios were tested in the dataset.

Within this dataset, seen in Figure 4.14, no consistent trend is resolved when considering only the classes. Instead, the activation barrier correlates strongly with the final NEB reaction coordinate (cumulative path length along the minimum-energy path): longer 48f $\rightarrow$ 48f paths systematically exhibit higher barriers. Consistent with this finding, traces in Figure 4.14 are not labeled by local environment; the figure emphasizes the dominant geometric (path-length) dependence observed in the present sample.

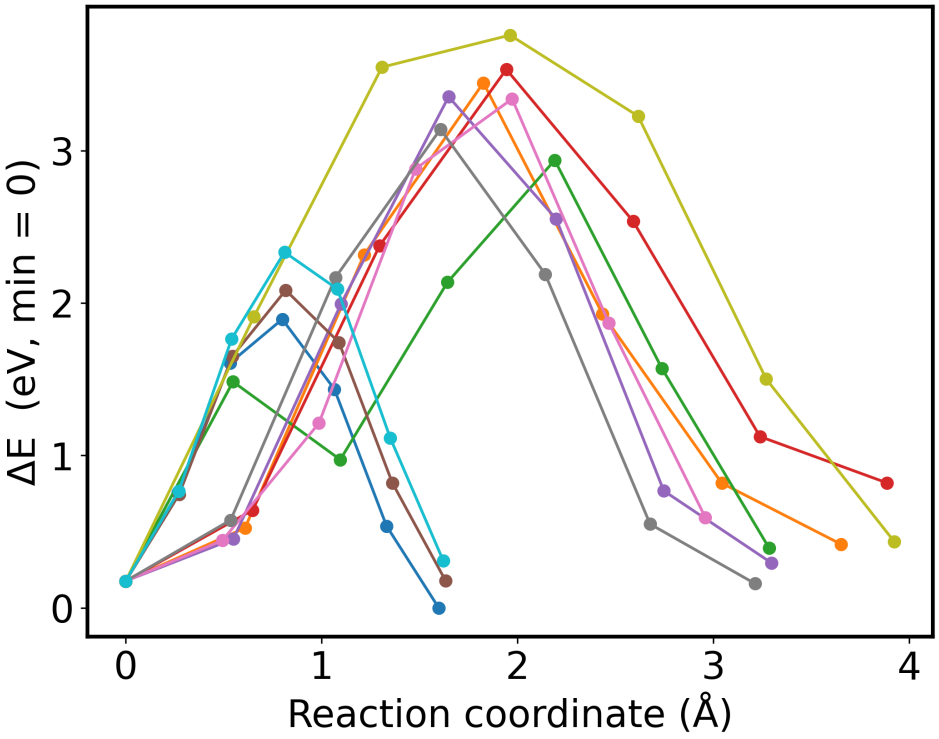


**Figure 4.14:** Energy barriers for hydrogen migration along various 48f–48f diffusion paths for various Li-H-Ti-O compositions.

Several specific start–end combinations were sampled at most once ($LiO_4 \rightarrow TiO_6$, $LiO_6 \rightarrow TiO_6$, $LiO_6 \rightarrow LiO_6$, $LiO_6 \rightarrow LiO_4$), so potential interaction effects between these particular pairs cannot be ruled out. For example, having three hops that all start on $LiO_6$ but terminate on three different end classes does not establish that "$LiO_6$ origins show no trend"; it only shows no trend at the single-factor level. Additionally, repeated NEB calculations for missing matched start–end pairs are required to test for pair-specific trends.

The NEB analysis reveals several key aspects of $Li^+$ and $H^+$ mobility during hydrogen-assisted delithiation that are directly relevant to the performance of spinel LTO as a lithium ion sieve.

The identification of the 8a $\rightarrow$ 16c $\rightarrow$ 8a and 16d $\rightarrow$ 16c $\rightarrow$ 8a routes as having lower activation energies than direct hops is particularly important. It demonstrates that the 16c site serves as a true kinetic "bridge" in the migration network, enabling $Li^+$ to bypass the high barriers of direct hops. This suggests that strategies to enlarge or stabilize the 16c site could further lower migration barriers and enhance $Li^+$ migration rates during sieving. This has been done for other spinels with intermediate 16c sites. For instance, applying tensile strain to the lattice of (Li, Al) codoped magnesium spinel has been shown to reduce $Li^+$ diffusion barriers by increasing the volumes of the transitional octahedral sites [84].

Even when accessed via 16c, 16d sites remain relatively inert, with barriers around 1.5 eV for $Li^+$ escape. While this does not directly limit $Li^+$ recovery in the pristine structure, since the active diffusion network could reside in the tetrahedral sublattices, it highlights that structural changes that promote $Li^+$ occupation of 16d sites could slow exchange kinetics and sieve efficiency. Controlling synthesis and operational conditions to minimize $Li^+$ trapping in octahedral sites could therefore be beneficial for maintaining high sieving rates. The magnitude of the LTO 16d-related barriers is consistent with values reported for lithium-ion sieves based on spinel LMO in comparable computational studies, which align with experimental observations that octahedral Li in LMO sieves are very difficult to leach [70]. By structural analogy, it is reasonable to expect that fully extracting 16d Li from spinel LTO will likewise be inefficient. A pragmatic implication is to terminate delithiation once the 8a network is depleted, leaving any residual 16d Li in place.

For $H^+$, no clear dependence on local cation environment was resolved in the current dataset, but a

strong geometric effect emerged: longer 48f $\rightarrow$ 48f paths consistently exhibited higher barriers, with the relationship appearing highly linear ($R^2 = 0.92$). This suggests that, at least in the sampled compositions, hydrogen mobility is governed more by path geometry than by chemical coordination. Even the lowest 48f $\rightarrow$ 48f barrier (1.90 eV) in the present dataset far exceeds the Li 8a–8a (via-16c) barriers. Due to the rate, $\sim \nu \exp(-E_a/k_B T)$, being energy barrier dependent, higher $H^+$ barriers imply slower characteristic times than $Li^+$ motion, assuming comparable attempt frequencies. Therefore, it may be reasonable to conclude that $H^+$ migration is more time-consuming than that of $Li^+$ and can act as the rate-limiting step of the ion-exchange cycle. This suggests that accelerating $H^+$ mobility, for instance by manipulating polyhedral tilts and linkage angles to shorten the paths, is highly relevant to speeding up the process.

It should also be noted that even the lowest calculated $H^+$ barrier (1.90 eV) remains very high. This may indicate that the present sampling of diffusion paths is incomplete, and that additional intermediate sites, analogous to the 16c site in Li migration, play a role in lowering the effective barriers for hydrogen diffusion. Identifying and testing such alternative pathways will be essential for establishing a more accurate picture of proton transport in this structure.

# 5

# Recommendations

This chapter outlines how the present work on spinel lithium titanium oxide (LTO) for lithium recovery can be extended and strengthened. It prioritizes actions that quantify and accelerate the ion-exchange cycle, improve methodological rigor and comparability of the computations, and translate atomistic insights into material and process designs.

A major challenge highlighted in the literature is that LTO sieves often require up to a full day to reach adsorption and desorption equilibrium, which constrains throughput and thereby economics. Any future program should therefore treat speed as a primary design objective.

The NEB results of this study indicate that $Li^+$ diffusion between adjacent 8a sites proceeds preferentially via the 16c intermediate (8a $\rightarrow$ 16c $\rightarrow$ 8a), while $Li^+$ escape from 16d is comparatively inert even via 16c. Thus 16c is a true kinetic bridge, whereas 16d-resident Li is difficult to leach.

Proton mobility also appears rate-limiting. $H^+$ migration barriers are high in the sampled paths and correlate strongly with path length, suggesting that $H^+$ motion can throttle the overall exchange cycle.

Another major limitation is that spinel LTO sieves perform poorly in acidic brines. Competition between protons and lithium ions at the exchange sites reduces uptake capacity and selectivity, limiting applicability in environments that are acidic.

To move beyond static, 0 K barriers and toward experimentally relevant timescales, future work should integrate explicit kinetic modeling. One promising direction is the use of ab initio or classical molecular dynamics to extract $Li^+$ and $H^+$ diffusivities across compositions and temperatures. Another is Kinetic Monte Carlo, where simulations on a network of NEB-characterized hops could be used to predict macroscopic exchange times and identify rate-controlling links.

Future work should also refine the methodological basis of the calculations. Rebuilding the delithiation and H-substitution datasets with symmetry-aware enumeration and structure-matching de-duplication, rather than large random draws, would avoid duplicates and yield cleaner statistics. The number of NEB runs should be increased to replicate the same path classes multiple times, enabling variance estimates and trend testing. These runs should also be extended to higher-Li compositions to examine how crowding and site occupancy modulate barriers. More rigorous approaches such as climbing-image NEB could be employed to ensure that the highest-energy image converges on the true saddle point, providing more accurate activation barriers. Finally, the high barriers observed for $H^+$ suggest that additional intermediate sites may exist. Systematic probing of such sites, supported by automated saddle-point searches, could reveal missing intermediates that lower barriers.

There are several material-level strategies worth pursuing. Enhancing $H^+$ mobility could be attempted through doping, strain, or defect engineering that shortens migration path lengths. Lattice-expanding strategies such as tensile strain or suitable dopants may improve access to the 16c site for $Li^+$. Controlling 16d occupancy by minimizing trapping on these sites, or by terminating delithiation once the 8a network is depleted, could also improve kinetics. Finally, dopants shown to be promising in related

systems—such as Zr, La, Mo, Fe, and Ni—should be systematically screened, with explicit attention to their effects on both $Li^+$ pathways and H-O affinity.

Attention should also be given to operating conditions. Moderate temperature increases may suppress any residual two-phase regions and reinforce solid-solution delithiation, and controlled experiments should test the need for or effect of this. Modeling and experiments should be extended to neutral and acidic conditions, including $Mg^{2+}$ competition, to reflect real brines and identify operating windows where LTO selectivity remains acceptable. Regeneration steps should be designed to re-disperse lithium and avoid unfavorable clustered states that could slow kinetics.

Lithium recovery from low-grade brines is inherently expensive, so the economic viability of any ion-sieve depends on two possible routes: either the material must be made cheap enough to allow deployment of a very large number of sieves in parallel, or the sieving process must be accelerated so that each unit cycles much faster. Both paths are demanding: large-scale production requires sustainable and low-cost synthesis methods, while faster kinetics require breakthroughs in ion mobility and exchange pathways. Future efforts must also balance improvements in speed, selectivity, and stability. Modifications that accelerate ion motion may affect Li/Mg selectivity or structural robustness, requiring co-optimization. Handling acidic brines will remain a challenge and may require combining LTO with other materials or hybrid process designs. Scale-up and sustainability also remain non-trivial, and low-impact synthesis routes should be developed in parallel with performance work.

In summary, future work should measure ion exchange speed, remove methodological noise through duplicate-free enumeration and denser, matched NEB sets, engineer $H^+$ mobility and open sites via doping or microstructure control, and use temperature and chemistry as levers to ensure solid-solution delithiation and sustain faster cycles. Finally, the economic barrier requires either developing ultra-low-cost synthesis routes for large-scale deployment or enabling much faster exchange cycles so that fewer sieves are needed. These steps directly address the current kinetic, chemical, and economic challenges and align with the thermodynamic picture developed here.

# 6

# Conclusion

This thesis combined a literature study with density functional theory (DFT) to evaluate spinel lithium titanium oxide ($Li_4Ti_5O_{12}$, LTO) as a lithium-ion sieve for recovery from complex brines. The work addressed two objectives: establish the phase stability and electrochemical response of LTO during lithium extraction with proton incorporation, and identify and quantify atomistic $Li^+$ and $H^+$ migration mechanisms, linking rate-limiting steps to site preferences and lattice features.

The literature review revealed that global lithium demand is rising while conventional supply routes face material, environmental, and cost constraints. Alternative sources such as geothermal and oil-field brines, seawater, and battery leachates present diverse chemistries and logistics; however, low lithium levels and high Mg/Li ratios commonly challenge viable recovery. As a result, sorption and ion-exchange media have emerged as promising, with titanium-based sieves favored for their structural robustness and benign chemistry. Lithium extraction in Ti-based sieves is typically operated via acid treatment, where Li is substituted with H to form protonated phases. This process sets the context for modeling hydrogen incorporation in LTO.

DFT thermodynamics show that hydrogen substitution stabilizes delithiated spinel LTO frameworks relative to vacancy counterparts: at like Li contents, H-substituted configurations have lower total energy and voltage penalties during delithiation, and the corresponding convex hull is indicative of solid-solution behavior with only shallow tielines. This stabilization is consistent across compositions and supports practical ion-exchange operation where protons replace lithium. In other words, proton incorporation stabilizes the supercell and aligns with how Ti-based sieves are used in practice. Beyond energetics, the structural response remains near zero-strain when hydrogen participates: protonation mitigates lattice expansion during delithiation, while Li clustering amplifies volume changes. Thus, homogeneous lithiation and controlled protonation are practical levers for durability.

Minimum-energy paths mapped via NEB revealed a clear kinetic hierarchy for lithium. The 8a $\rightarrow$ 16c $\rightarrow$ 8a path is the preferred route between adjacent tetrahedra, with 16c acting as a kinetic bridge that lowers barriers compared to direct 8a$\rightarrow$ 8a hops. By contrast, $Li^+$ escape from 16d remains comparatively inert, implying that delithiation should be operated to deplete the tetrahedral 8a network rather than target residual octahedral Li, which would be slow to leach. For proton transport, NEB calculations showed substantially higher barriers than for lithium and a strong dependence on path length along 48f $\rightarrow$ 48f trajectories. Longer geometric paths consistently incurred larger activation energies. The present dataset does not indicate a dependence on the local cation environment; instead, geometry dominates, and proton mobility is a likely rate-limiting step during ion exchange.

Taken together, the thermodynamic and kinetic results reconcile the practical picture that emerged from the literature. LTO stays structurally resilient across Li/H compositions, with proton substitution stabilizing delithiated frameworks and helping maintain near-zero strain, advantages for cycling stability and mechanical integrity. At the same time, proton diffusion pathways are intrinsically slower, creating a bottleneck that matches reports of sluggish adsorption–desorption and alkaline operating windows.

Three design levers emerge from this study. First, amplifying the 16c bridge for lithium, for example, through lattice expansion via dopants or strain, can secure a faster $Li^+$ network. Second, shortening proton paths or lowering $H^+$ barriers again through doping, strain, or defect engineering could directly address the geometric control observed in NEB and improve rate performance. Third, operating conditions should preserve homogeneity and avoid Li clustering to maintain near-zero-strain behavior and thermodynamic smoothness.

Methodologically, additional $H^+$ intermediates should be probed to identify potentially lower-barrier routes. Finite-temperature free energies and explicit brine environments will close realism gaps. Kinetic modeling could translate barriers into cycle times, directly targeting the day-long exchanges cited in experiments.

In conclusion, this work (i) establishes that LTO remains thermodynamically and structurally robust during lithium extraction with hydrogen substitution, with H stabilizing delithiated frameworks and promoting near-zero-strain behavior, and (ii) identifies a kinetic asymmetry in which lithium leverages a 16c-mediated network while proton mobility, governed by path length, likely limits exchange rates. These insights, grounded in practical ion-exchange operation, supply a basis for rational improvements and set a computational-experimental agenda to deliver faster, selective, and durable lithium recovery from challenging brines.

# References


[1] Majid Alipanah et al. “Value recovery from spent lithium-ion batteries: A review on technologies, environmental impacts, economics, and supply chain”. In: *Clean Technologies and Recycling* 1 (Dec. 2021), pp. 152–184.

[2] F M Nizam Uddin Khan et al. “Design and optimization of lithium-ion battery as an efficient energy storage device for electric vehicles: A comprehensive review”. In: *Journal of Energy Storage* 71 (2023), p. 108033. ISSN: 2352-152X. URL: https://www.sciencedirect.com/science/article/pii/S2352152X23014305.

[3] France. *Lithium: The White Gold of the Energy Transition*. Nov. 30, 2023. URL: https://webdoc.france24.com/lithium-energy-automobile-industry-bolivia-argentina-chile/.

[4] TalkMarkets. *Lithium: A Commodity in Perpetual Deficit*. Accessed: 2025-03-24. n.d. URL: https://talkmarkets.com/content/commodities/lithium-a-commodity-in-perpetual-deficit?post=324023.

[5] Sun Han et al. “Global supply sustainability assessment of critical metals for clean energy technology”. In: *Resources Policy* 85 (2023), p. 103994. ISSN: 0301-4207. URL: https://www.sciencedirect.com/science/article/pii/S0301420723007055.

[6] Benchmark Source. *Hard Rock Lithium vs. Brine - How Do Their Carbon Curves Compare?* https://source.benchmarkminerals.com/article/hard-rock-vs-brine-how-do-their-carbon-curves-compare. Accessed: 2025-03-13. n.d.

[7] Lingjie Zhang et al. “Adsorbents for lithium extraction from salt lake brine with high magnesium/lithium ratio: From structure-performance relationship to industrial applications”. In: *Desalination* 579 (2024), p. 117480. ISSN: 0011-9164. URL: https://www.sciencedirect.com/science/article/pii/S0011916424001917.

[8] Jianpeng Sun et al. “Recent Advances in Lithium Extraction Using Electrode Materials of Li-Ion Battery from Brine/Seawater”. In: *Processes* 10.12 (2022). ISSN: 2227-9717. URL: https://www.mdpi.com/2227-9717/10/12/2654.

[9] Yanan Pan, Weiquan Zhan, and Wencai Zhang. “Advanced computational strategies for lithium chemical and electrochemical adsorption: A comprehensive state-of-the-art review”. In: *Desalination* 600 (2025), p. 118524. ISSN: 0011-9164. URL: https://www.sciencedirect.com/science/article/pii/S0011916424012359.

[10] Bo Xu and Ying Meng. “Factors affecting Li mobility in spinel LiMn 2O 4—A first-principles study by GGA and GGA+ U methods”. In: *Journal of Power Sources - J POWER SOURCES* 195 (Aug. 2010), pp. 4971–4976.

[11] Mengxiang Lu et al. “DFT calculation and experiments for Li+/H+ ion-exchange on titanium-based lithium ion-sieves”. In: *Chemical Engineering Science* 300 (2024), p. 120619. ISSN: 0009-2509. URL: https://www.sciencedirect.com/science/article/pii/S0009250924009199.

[12] Basudev Swain. “Recovery and recycling of lithium: A review”. In: *Separation and Purification Technology* 172 (2017), pp. 388–403. ISSN: 1383-5866. URL: https://www.sciencedirect.com/science/article/pii/S1383586616305652.

[13] David Torres et al. “Salar de Atacama Lithium and Potassium Productive Process”. In: *Metals* 14.10 (2024). ISSN: 2075-4701. URL: https://www.mdpi.com/2075-4701/14/10/1095.

[14] Bernard Sanjuan et al. “Lithium-rich geothermal brines in Europe: An up-date about geochemical characteristics and implications for potential Li resources”. In: *Geothermics* 101 (2022), p. 102385. ISSN: 0375-6505. URL: https://www.sciencedirect.com/science/article/pii/S0375650522000372.

[15] Ewa Knapik, Grzegorz Rotko, and Marta Marszałek. “Recovery of Lithium from Oilfield Brines—Current Achievements and Future Perspectives: A Mini Review”. In: *Energies* 16 (Sept. 2023), p. 6628.

[16] Samihah Zura Mohd Nani et al. “Potential Health Benefits of Deep Sea Water: A Review”. In: *Evidence-Based Complementary and Alternative Medicine* 2016 (Dec. 2016), pp. 1–18.

[17] Basudev Swain et al. “Hydrometallurgical process for recovery of cobalt from waste cathodic active material generated during manufacturing of lithium ion batteries”. In: *Journal of Power Sources* 167.2 (2007), pp. 536–544. ISSN: 0378-7753. URL: https://www.sciencedirect.com/science/article/pii/S0378775307004600.

[18] Tedd E. Lister et al. *Separation of Cobalt, Nickel, and Manganese in Leach Solutions of Waste Lithium-Ion Batteries Using Dowex M4195 Ion Exchange Resin*. Tech. rep. INL/JOU-21-65504-Revision-0. Prepared for the U.S. Department of Energy under DOE Idaho Operations Office Contract DE-AC07-05ID14517. Idaho Falls, Idaho, USA: Idaho National Laboratory, 2021. URL: https://www.osti.gov/servlets/purl/1897968.

[19] Yafei Jie et al. “Thermodynamic Analysis and Experimental Investigation of Al and F Removal from Sulfuric Acid Leachate of Spent LiFePO4 Battery Powder”. In: *Metals* 11 (Oct. 2021), p. 1641.

[20] Victoria Flexer, Celso Fernando Baspineiro, and Claudia Inés Galli. “Lithium recovery from brines: A vital raw material for green energies with a potential environmental impact in its mining and processing”. In: *Science of The Total Environment* 639 (2018), pp. 1188–1204. ISSN: 0048-9697. URL: https://www.sciencedirect.com/science/article/pii/S0048969718318746.

[21] T. Georgi-Maschler et al. “Development of a recycling process for Li-ion batteries”. In: *Journal of Power Sources* 207 (2012), pp. 173–182. ISSN: 0378-7753. URL: https://www.sciencedirect.com/science/article/pii/S0378775312002984.

[22] Zhongwei Zhao et al. “Li extraction from high Mg/Li ratio brine with LiFePO4/FePO4 as electrode materials”. In: *Hydrometallurgy* 133 (2013), pp. 75–83. ISSN: 0304-386X. URL: https://www.sciencedirect.com/science/article/pii/S0304386X12002538.

[23] Thomas R. Benson, Matthew A. Coble, and John H. Dilles. “Hydrothermal enrichment of lithium in intracaldera illite-bearing claystones”. In: *Science Advances* 9.35 (2023), eadh8183. eprint: https://www.science.org/doi/pdf/10.1126/sciadv.adh8183. URL: https://www.science.org/doi/abs/10.1126/sciadv.adh8183.

[24] Peter Bayer et al. “Review on life cycle environmental effects of geothermal power generation”. In: *Renewable and Sustainable Energy Reviews* 26 (2013), pp. 446–463. ISSN: 1364-0321. URL: https://www.sciencedirect.com/science/article/pii/S1364032113003420.

[25] Vanessa Schenker et al. “Is lithium from geothermal brines the sustainable solution for Li-ion batteries?” In: *Renewable and Sustainable Energy Reviews* 199 (2024), p. 114456. ISSN: 1364-0321. URL: https://www.sciencedirect.com/science/article/pii/S1364032124001795.

[26] Ebenezer T. Igunnu and George Z. Chen. “Produced water treatment technologies”. In: *International Journal of Low-Carbon Technologies* 9.3 (July 2012), pp. 157–177. ISSN: 1748-1317. eprint: https://academic.oup.com/ijlct/article-pdf/9/3/157/9644076/cts049.pdf. URL: https://doi.org/10.1093/ijlct/cts049.

[27] Tutuk Djoko Kusworo et al. “Oilfield produced water treatment to clean water using integrated activated carbon-bentonite adsorbent and double stages membrane process”. In: *Chemical Engineering Journal* 347 (2018), pp. 462–471. ISSN: 1385-8947. URL: https://www.sciencedirect.com/science/article/pii/S1385894718307095.

[28] Xin He, Sumanjeet Kaur, and Robert Kostecki. “Mining Lithium from Seawater”. In: *Joule* 4.7 (2020), pp. 1357–1358. ISSN: 2542-4351. URL: https://www.sciencedirect.com/science/article/pii/S2542435120302786.

[29] Xin Zhang et al. “A Review of Resource Recovery from Seawater Desalination Brine”. In: *Reviews in Environmental Science and Bio/Technology* 20.2 (2021), pp. 333–361. ISSN: 1572-9826. URL: https://doi.org/10.1007/s11157-021-09570-4.

[30] Edward Jones et al. “The state of desalination and brine production: A global outlook”. In: *Science of The Total Environment* 657 (2019), pp. 1343–1356. ISSN: 0048-9697. URL: https://www.sciencedirect.com/science/article/pii/S0048969718349167.

[31] Mengyuan Chen et al. “Recycling End-of-Life Electric Vehicle Lithium-Ion Batteries”. In: *Joule* 3.11 (2019), pp. 2622–2646. ISSN: 2542-4351. URL: https://www.sciencedirect.com/science/article/pii/S254243511930474X.

[32] H. Wang et al. “Recovery of Li and Co in Waste Lithium Cobalt Oxide-Based Battery Using H1.6Mn1.6O4”. In: *Molecules* 28.9 (Apr. 2023), p. 3737.

[33] Xiaohong Zheng et al. “A Mini-Review on Metal Recycling from Spent Lithium Ion Batteries”. In: *Engineering* 4.3 (2018), pp. 361–370. ISSN: 2095-8099. URL: https://www.sciencedirect.com/science/article/pii/S2095809917308226.

[34] Xianfeng Hu, Elsayed Mousa, and Guozhu Ye. “Recovery of Co, Ni, Mn, and Li from Li-ion batteries by smelting reduction - Part II: A pilot-scale demonstration”. In: *Journal of Power Sources* 483 (2021), p. 229089. ISSN: 0378-7753. URL: https://www.sciencedirect.com/science/article/pii/S0378775320313847.

[35] Richard Woeste et al. “A techno-economic assessment of two recycling processes for black mass from end-of-life lithium-ion batteries”. In: *Applied Energy* 361 (2024), p. 122921. ISSN: 0306-2619. URL: https://www.sciencedirect.com/science/article/pii/S0306261924003040.

[36] Xin Xu et al. “Extraction of lithium with functionalized lithium ion-sieves”. In: *Progress in Materials Science* 84 (2016), pp. 276–313. ISSN: 0079-6425. URL: https://www.sciencedirect.com/science/article/pii/S0079642516300615.

[37] O. Murphy and M. N. Haji. “A Review of Technologies for Direct Lithium Extraction from Low $Li^+$ Concentration Aqueous Solutions”. In: *Frontiers in Chemical Engineering* 4 (2022). URL: https://doi.org/10.3389/fceng.2022.1008680.

[38] Shulei Wang et al. “Lithium adsorption from brine by iron-doped titanium lithium ion sieves”. In: *Particuology* 41 (2018), pp. 40–47. ISSN: 1674-2001. URL: https://www.sciencedirect.com/science/article/pii/S1674200118300944.

[39] Suyu Zhou et al. “Zr-doped titanium lithium ion sieve and EP-granulated composite: Superb adsorption and recycling performance”. In: *Particuology* 69 (2022), pp. 100–110. ISSN: 1674-2001. URL: https://www.sciencedirect.com/science/article/pii/S1674200121002406.

[40] Laura Vega Garcia et al. “Lithium in a Sustainable Circular Economy: A Comprehensive Review”. In: *Processes* 11.2 (2023). ISSN: 2227-9717. URL: https://www.mdpi.com/2227-9717/11/2/418.

[41] Abdullah Khalil et al. “Lithium recovery from brine: Recent developments and challenges”. In: *Desalination* 528 (2022), p. 115611. ISSN: 0011-9164. URL: https://www.sciencedirect.com/science/article/pii/S0011916422000662.

[42] Thines Kanagasundaram et al. “The recovery and separation of lithium by using solvent extraction methods”. In: *Coordination Chemistry Reviews* 509 (2024), p. 215727. ISSN: 0010-8545. URL: https://www.sciencedirect.com/science/article/pii/S0010854524000730.

[43] J. F. Song et al. “Lithium Extraction from Chinese Salt-Lake Brines: Opportunities, Challenges, and Future Outlook”. In: *Environmental Science: Water Research Technology* 3.4 (2017), pp. 593–597. URL: https://doi.org/10.1039/c7ew00020k.

[44] Xianhui Li et al. “Membrane-based technologies for lithium recovery from water lithium resources: A review”. In: *Journal of Membrane Science* 591 (2019), p. 117317. ISSN: 0376-7388. URL: https://www.sciencedirect.com/science/article/pii/S037673881930095X.

[45] A. Somrani, A.H. Hamzaoui, and M. Pontie. “Study on lithium separation from salt lake brines by nanofiltration (NF) and low pressure reverse osmosis (LPRO)”. In: *Desalination* 317 (2013), pp. 184–192. ISSN: 0011-9164. URL: https://www.sciencedirect.com/science/article/pii/S0011916413001252.

[46] Jiuyun Cui et al. “Synthesis of cauliflower-like ion imprinted polymers for selective adsorption and separation of lithium ion”. In: *New Journal of Chemistry* 42.17 (2018), pp. 14502–14509.

[47] Jing Zhong, Sen Lin, and Jianguo Yu. “Li+ adsorption performance and mechanism using lithium/aluminum layered double hydroxides in low grade brines”. In: *Desalination* 505 (2021), p. 114983. ISSN: 0011-9164. URL: https://www.sciencedirect.com/science/article/pii/S0011916421000540.

[48] Mingzhe Dong et al. “Lithium adsorption properties of porous LiAl-layered double hydroxides synthesized using surfactants”. In: *Journal of Saudi Chemical Society* 26.5 (2022), p. 101535. ISSN: 1319-6103. URL: https://www.sciencedirect.com/science/article/pii/S131961032200117X.

[49] Yuanyuan Li et al. “Fabrication of Fe-doped lithium-aluminum-layered hydroxide chloride with enhanced reusable stability inspired by computational theory and its application in lithium extraction”. In: *Colloids and Surfaces A: Physicochemical and Engineering Aspects* 658 (2023), p. 130641. ISSN: 0927-7757. URL: https://www.sciencedirect.com/science/article/pii/S0927775722023962.

[50] Ping Xu et al. “Materials for Lithium Recovery from Salt Lake Brine”. In: *Journal of Materials Science* 56.1 (2021), pp. 16–63. ISSN: 1573-4803. URL: https://doi.org/10.1007/s10853-020-05019-1.

[51] Yothin Chimupala. “Synthesis and characterization of the TiO2(B) phase”. In: 2015. URL: https://api.semanticscholar.org/CorpusID:138843336.

[52] Shudan Wei et al. “Porous Lithium Ion Sieves Nanofibers: General Synthesis Strategy and Highly Selective Recovery of Lithium from Brine Water”. In: *Chemical Engineering Journal* 379 (Aug. 2019), p. 122407.

[53] Shulei Wang et al. “High adsorption performance of the Mo-doped titanium oxide sieve for lithium ions”. In: *Hydrometallurgy* 187 (2019), pp. 30–37. ISSN: 0304-386X. URL: https://www.sciencedirect.com/science/article/pii/S0304386X19302002.

[54] Shulei Wang et al. “Superior lithium adsorption and required magnetic separation behavior of iron-doped lithium ion-sieves”. In: *Chemical Engineering Journal* 332 (2018), pp. 160–168. ISSN: 1385-8947. URL: https://www.sciencedirect.com/science/article/pii/S1385894717315541.

[55] Ju Miao et al. “Novel LIS-doped mixed matrix membrane absorbent with high structural stability for sustainable lithium recovery from geothermal water”. In: *Desalination* 527 (2022), p. 115570. ISSN: 0011-9164. URL: https://www.sciencedirect.com/science/article/pii/S001191642200025X.

[56] Lu Zheng et al. “Highly selective lanthanide-doped ion sieves for lithium recovery from aqueous solutions”. In: *Journal of Chemical Research* 47.2 (2023), p. 17475198231159051. eprint: https://doi.org/10.1177/17475198231159051. URL: https://doi.org/10.1177/17475198231159051.

[57] Jin Cheng et al. “Hierarchical Hollow $Li_4Ti_5O_{12}$ Urchin-like Microspheres with Ultra-high Specific Surface Area for High Rate Lithium Ion Batteries”. In: *Nano Research* 7.7 (2014), pp. 1043–1053. ISSN: 1998-0000. URL: https://doi.org/10.1007/s12274-014-0467-2.

[58] Na Li et al. “Yolk-shell structured composite for fast and selective lithium ion sieving”. In: *Journal of Colloid and Interface Science* 520 (2018), pp. 33–40. ISSN: 0021-9797. URL: https://www.sciencedirect.com/science/article/pii/S0021979718301796.

[59] Xiaowei Li et al. “Highly selective separation of lithium with hierarchical porous lithium-ion sieve microsphere derived from MXene”. In: *Desalination* 537 (2022), p. 115847. ISSN: 0011-9164. URL: https://www.sciencedirect.com/science/article/pii/S0011916422003022.

[60] Xinghong Pu et al. “Interface and defect engineering enable fast and high-efficiency Li extraction of metatitanic acid adsorbent”. In: *Chemical Engineering Journal* 425 (2021), p. 130550. ISSN: 1385-8947. URL: https://www.sciencedirect.com/science/article/pii/S1385894721021367.

[61] Bing Zhao et al. “Unraveling the Li+ desorption behavior and mechanism of Li4Ti5O12 with different facets to enhance lithium extraction”. In: *J. Mater. Chem. A* 11 (13 2023), pp. 7094–7104. URL: http://dx.doi.org/10.1039/D2TA10016A.

[62] Bing Zhao et al. “The performance and mechanism of recovering lithium on H4Ti5O12 adsorbents influenced by (110) and (111) facets exposed”. In: *Chemical Engineering Journal* 414 (2021), p. 128729. ISSN: 1385-8947. URL: https://www.sciencedirect.com/science/article/pii/S1385894721003272.

[63] David S. Sholl and Janice A. Steckel. “What is Density Functional Theory?” In: *Density Functional Theory*. John Wiley & Sons, Ltd, 2009. Chap. 1, pp. 1–33. ISBN: 9780470447710. eprint: https://onlinelibrary.wiley.com/doi/pdf/10.1002/9780470447710.ch1. URL: https://onlinelibrary.wiley.com/doi/abs/10.1002/9780470447710.ch1.

[64] Init.At. *About*. Accessed: 2025-03-24. n.d. URL: https://www.vasp.at/info/about/.

[65] Quantum ESPRESSO. *Manifesto - Quantum Espresso*. Accessed: 2025-03-24. Jan. 26, 2024. URL: https://www.quantum-espresso.org/manifesto/.

[66] GPAW. *GPAW: DFT and Beyond within the Projector-Augmented Wave Method*. Accessed: 2025-03-24. n.d. URL: https://gpaw.readthedocs.io/.

[67] CASTEP. *Homepage | CASTEP*. Accessed: 2025-03-24. n.d. URL: https://www.castep.org/.

[68] FHI-aims. *Learn More about FHI-aims*. Accessed: 2025-03-24. URL: https://fhi-aims.org/learn-more.

[69] The SIESTA Group. *SIESTA: Efficient electronic structure calculations and ab initio molecular dynamics*. Accessed: 2025-03-24. n.d. URL: https://siesta-project.org/siesta/About/overview.html.

[70] Aolei Gao et al. “Lithium-desorption mechanism in LiMn2O4, Li1.33Mn1.67O4, and Li1.6Mn1.6O4 according to precisely controlled acid treatment and density functional theory calculations”. In: *J. Mater. Chem. A* 7 (36 2019), pp. 20878–20890. URL: http://dx.doi.org/10.1039/C9TA06080D.

[71] Guotai Zhang et al. “Synergistic doping and coating of lithium ion-sieves for enhanced lithium recovery from brine”. In: *Desalination* 601 (2025), p. 118556. ISSN: 0011-9164. URL: https://www.sciencedirect.com/science/article/pii/S0011916425000311.

[72] Jing Liu et al. “Design and adsorption performance of hollow structure nano-metatitanic acid lithium ion sieve with strong structure stability and large adsorption capacity”. In: *Colloids and Surfaces A: Physicochemical and Engineering Aspects* 692 (2024), p. 133960. ISSN: 0927-7757. URL: https://www.sciencedirect.com/science/article/pii/S0927775724008215.

[73] Hsieh Chen. “Phase transitions limit lithium adsorption in titanium-based ion sieves”. In: *Materials Today Physics* 46 (2024), p. 101508. ISSN: 2542-5293. URL: https://www.sciencedirect.com/science/article/pii/S2542529324001846.

[74] *Category:INCAR tag - VASP Wiki*. https://www.vasp.at/wiki/index.php/Category:INCAR_tag. Accessed: 2025-05-07. n.d.

[75] Lkhagvajav Sarantuya et al. “Synthesis, Structure and Electronic Properties of Li4Ti5O12 Anode Material for Lithium Ion Batteries”. In: *Solid State Phenomena* 271 (Jan. 2018), pp. 9–17.

[76] Haodong Liu et al. “Elucidating the Limit of Li Insertion into the Spinel $Li_4Ti_5O_{12}$”. In: *ACS Materials Letters* 1.1 (2019), pp. 96–102. URL: https://doi.org/10.1021/acsmaterialslett.9b00099.

[77] Alexandros Vasileiadis et al. “Ab Initio Study of Sodium Insertion in the $\lambda$-$Mn_2O_4$ and Dis/Ordered $\lambda$-$Mn_{1.5}Ni_{0.5}O_4$ Spinels”. In: *Chemistry of Materials* 30.19 (2018), pp. 6646–6659. ISSN: 0897-4756. URL: https://doi.org/10.1021/acs.chemmater.8b01634.

[78] Graeme Henkelman, Blas P. Uberuaga, and Hannes Jónsson. “A climbing image nudged elastic band method for finding saddle points and minimum energy paths”. In: *The Journal of Chemical Physics* 113.22 (Dec. 2000), pp. 9901–9904. ISSN: 0021-9606. eprint: https://pubs.aip.org/aip/jcp/article-pdf/113/22/9901/19259681/9901_1_online.pdf. URL: https://doi.org/10.1063/1.1329672.

[79] Graeme Henkelman and Hannes Jónsson. “Improved tangent estimate in the nudged elastic band method for finding minimum energy paths and saddle points”. In: *The Journal of Chemical Physics* 113.22 (Dec. 2000), pp. 9978–9985. ISSN: 0021-9606. eprint: https://pubs.aip.org/aip/jcp/article-pdf/113/22/9978/19260728/9978_1_online.pdf. URL: https://doi.org/10.1063/1.1323224.

[80] S. Lkhagvajav et al. “Structural and electronic properties of the spinel $Li_4Ti_5O_{12}$”. In: *Mongolian Journal of Chemistry* 20.46 (2019), pp. 7–12. URL: https://doi.org/10.5564/mjc.v20i46.1236.

[81] Hye-min Kim et al. “Mixed anion effects on structural and electrochemical characteristics of Li4Ti5O12 for high-rate and durable anode materials”. In: *J. Mater. Chem. A* 12 (12 2024), pp. 7107–7121. URL: http://dx.doi.org/10.1039/D3TA03494A.

[82] Ziqi Wu et al. “Microscopic electrochemical–mechanical coupling in layered cathodes under high-voltage and fast-charging conditions”. In: *EES Batteries* 1 (1 2025), pp. 73–99. URL: http://dx.doi.org/10.1039/D4EB00022F.

[83] Swapna Ganapathy et al. “The Fine Line between a Two-Phase and Solid-Solution Phase Transformation and Highly Mobile Phase Interfaces in Spinel Li4+ xTi5O12”. English. In: *Advanced Energy Materials* (2017). Accepted Author Manuscript. ISSN: 1614-6832.

[84] Conn O’Rourke and Benjamin J. Morgan. “Interfacial strain effects on lithium diffusion pathways in the spinel solid electrolyte Li-doped $MgAl_2O_4$”. In: *Phys. Rev. Mater.* 2 (4 Apr. 2018), p. 045403. URL: https://link.aps.org/doi/10.1103/PhysRevMaterials.2.045403.